

Spatially resolved origin of mm-wave linear polarization in the nuclear region of 3C 84

J. -Y. Kim¹, T. P. Krichbaum¹, A. P. Marscher², S. G. Jorstad^{2,3}, I. Agudo⁴, C. Thum⁵, J. A. Hodgson⁶, N. R. MacDonald¹, E. Ros¹, R. -S. Lu^{1,7}, M. Bremer⁸, P. de Vicente⁹, M. Lindqvist¹⁰, S. Trippe¹¹, and J. A. Zensus¹

¹ Max-Planck Institut für Radioastronomie, Auf dem Hügel 69, 53121 Bonn, Germany
e-mail: jykim@mpi-fr-bonn.mpg.de

² Institute for Astrophysical Research, Boston University, 725 Commonwealth Avenue, Boston, MA 022, USA

³ Astronomical Institute, St. Petersburg State University, Universitetskij Pr. 28, Petrodvorets, 198504 St. Petersburg, Russia

⁴ Instituto de Astrofísica de Andalucía (CSIC), Apartado 3004, 18080, Granada, Spain

⁵ Instituto de Radio Astronomía Millimétrica, Avenida Divina Pastora, 7, Local 20, E-18012 Granada, Spain

⁶ Korea Astronomy and Space Science Institute, 776 Daedeokdae-ro, Yuseong-gu, Daejeon, 30455, Korea

⁷ Shanghai Astronomical Observatory, Chinese Academy of Sciences, 80 Nandan Road, Shanghai 200030, China

⁸ Institut de Radio Astronomie Millimétrique, 300 rue de la Piscine, Domaine Universitaire, Saint Martin d'Hères 38406, France

⁹ Observatorio de Yebes (IGN), Apartado 148, E-19180 Yebes, Spain

¹⁰ Department of Space, Earth and Environment, Chalmers University of Technology, Onsala Space Observatory, 439 92 Onsala, Sweden

¹¹ Department of Physics and Astronomy, Seoul National University, 1 Gwanak-ro, Gwanak-gu, Seoul 08826, Korea

Received –; accepted –

ABSTRACT

We report results from a deep polarization imaging of the nearby radio galaxy 3C 84 (NGC 1275). The source was observed with the Global Millimeter VLBI Array (GMVA) at 86 GHz at an ultra-high angular resolution of $50\mu\text{as}$ (corresponding to $250R_s$). We also add complementary multi-wavelength data from the Very Long Baseline Array (VLBA; 15 & 43 GHz) and from the Atacama Large Millimeter/submillimeter Array (ALMA; 97.5, 233.0, and 343.5 GHz). At 86 GHz, we measure a fractional linear polarization of $\sim 2\%$ in the VLBI core region. The polarization morphology suggests that the emission is associated with an underlying limb-brightened jet. The fractional linear polarization is lower at 43 and 15 GHz ($\sim 0.3 - 0.7\%$ and $< 0.1\%$, respectively). This suggests an increasing linear polarization degree towards shorter wavelengths on VLBI scales. We also obtain a large rotation measure (RM) of $\sim 10^{5-6}$ rad/m² in the core at ≥ 43 GHz. Moreover, the VLBA 43 GHz observations show a variable RM in the VLBI core region during a small flare in 2015. Faraday depolarization and Faraday conversion in an inhomogeneous and mildly relativistic plasma could explain the observed linear polarization characteristics and the previously measured frequency dependence of the circular polarization. Our Faraday depolarization modeling suggests that the RM most likely originates from an external screen with a highly uniform RM distribution. To explain the large RM value, the uniform RM distribution, and the RM variability, we suggest that the Faraday rotation is caused by a boundary layer in a transversely stratified jet. Based on the RM and the synchrotron spectrum of the core, we provide an estimate for the magnetic field strength and the electron density of the jet plasma.

Key words. Galaxies: active – Galaxies: jets – Galaxies: individual (NGC 1275, 3C 84) – Techniques: interferometric, polarimetric

1. Introduction

Magnetic fields in the vicinity of central black holes (BHs) could play a significant role in the formation, collimation, and acceleration of relativistic jets in active galactic nuclei (AGN) (e.g., Blandford & Znajek 1977; Blandford & Payne 1982). Polarization sensitive very long baseline interferometry (VLBI) is an important technique to study the topology and strength of the magnetic fields at the base of AGN jets. Synchrotron theory predicts linear polarization of up to $m_L \sim 70\%$ for optically thin emission and well ordered magnetic fields (Pacholczyk 1970). However, VLBI observations typically find much lower linear polarizations ($m_L \lesssim 5\%$) in the VLBI cores of AGN-jets (Lister & Homan 2005; Jorstad et al. 2007). The origin of the weak linear polarization may be due to (i) high synchrotron self-absorption opacity, (ii) a large Faraday depth (e.g., Taylor et al. 2006), and/or (iii) highly disordered magnetic fields within the observing beam, e.g., induced by a turbulent plasma (e.g.,

Marscher 2014). The observed linear polarization can be also reduced by bandwidth depolarization, if Faraday rotation is large. Observations at millimeter wavelengths help to overcome the opacity barrier and are less affected by Faraday depolarization than in the cm-bands. Furthermore, owing to its small beam size, VLBI observations at millimeter wavelengths (mm-VLBI) have a small in-beam depolarization, in comparison to single-dish or connected interferometer array observations. Thus mm-VLBI polarimetry is a suitable technique to observe and study the polarization properties of compact radio sources (see also Boccardi et al. 2017).

The radio galaxy 3C 84 (Perseus A, NGC 1275) is an intriguing source whose linear polarization in the core region at cm-wavelengths is extremely weak ($< 0.1\%$ at ≤ 15 GHz; Taylor et al. 2006). This is much lower than typically observed in other AGN jets (Lister & Homan 2005). 3C 84 is also a relatively nearby source at a redshift of $z = 0.0176$ and a luminosity

distance of $d_L = 75$ Mpc (Strauss et al. 1992)¹. The mass of its central supermassive black hole (SMBH) has been estimated to be $M_{\text{BH}} \sim 9 \times 10^8 M_\odot$ (Scharwächter et al. 2013). The combination of proximity and large black hole mass makes 3C 84 an ideal candidate to study the jet base and its polarization properties with the highest possible angular and spatial resolution, using global mm-VLBI. For the adopted distance an angular scale of $50 \mu\text{as}$ corresponds to a linear scale of ~ 0.0175 pc or ~ 203 Schwarzschild radii (R_s).

At 1.3 mm and 0.9 mm wavelengths (230 and 341 GHz), Plambeck et al. (2014) report a typical degree of linear polarization $m_L \gtrsim 1\%$ using the Combined Array for Research in Millimeter Astronomy (CARMA) and the Submillimeter Array (SMA) with arc-second scale angular resolution. The authors also find a large rotation measure of $\text{RM} \sim 9 \times 10^5 \text{ rad/m}^2$. IRAM 30m Telescope observations at 86 and 230 GHz reveal a typical $\text{RM} \sim 7 \times 10^4 \text{ rad/m}^2$ (Agudo et al. 2014, 2018b). Both Plambeck et al. (2014) and Agudo et al. (2018b) report polarization variability on monthly timescales at mm-wavelengths, implying a small emission region (apparent size $\lesssim 1 \text{ c} \times 1 \text{ month} \sim 0.025 \text{ pc} \sim 0.1 \text{ mas}$).

At cm-wavelengths and on milli-arcsecond scales, however, only low-level polarization is observed. As mentioned above, Very Long Baseline Array (VLBA) observations of the VLBI core of 3C 84 reveal a linear polarization of $m_L \lesssim 0.1\%$ at 15 GHz (upper limit) and $m_L \sim 0.2\%$ at 22 GHz (Taylor et al. 2006). It was suggested that Faraday depolarization with $\text{RM} \gtrsim 10^4 \text{ rad/m}^2$ could be an explanation (Taylor et al. 2006). The high RM is also consistent with the non-VLBI measurements (Plambeck et al. 2014; Agudo et al. 2018b). However, the limited angular resolution of the previous observations does not yet allow to precisely locate the polarized emission region nor unambiguously determine the physical origin of the high RM. Observations with the Global Millimeter-VLBI Array (GMVA) help to overcome this limitation. The observing frequency of 86 GHz nicely bridges the gap between the 5–22 GHz and 230 GHz observations. This will help to connect the results from the previous studies (e.g., Aller et al. 2003; Agudo et al. 2010; Trippe et al. 2012; Agudo et al. 2018a; Plambeck et al. 2014; Nagai et al. 2017), in order to form a self-consistent physical jet polarization model from the cm- to the mm-regime.

In this paper, we present a new study of the polarization properties of 3C 84 based on GMVA observations at 86 GHz and supplemented by close-in-time VLBA observations at 43 GHz and 15 GHz. In Sect. 2 we describe details of the VLBI observations and the data reduction. Our main findings from the observations are summarized in Sect. 3. The physical implications are discussed in Sect. 4. In Sect. 5 we summarize the results.

2. Observations & data reduction

2.1. GMVA 86 GHz data

3C 84 was observed with the GMVA at 86 GHz in dual circular polarization in May 2015. The source was observed as one of the γ -ray emitting AGN sources, which are monitored by semiannual GMVA observations that complement the VLBA-BU-BLAZAR monitoring program (Jorstad et al. 2017; for the GMVA monitoring see e.g., Rani et al. 2015; Hodgson et al. 2017; Casadio et al. 2017). In this GMVA campaign a total of 11 antennas observed 3C 84: Brewster (BR), Effelsberg (EB), Fort

Davis (FD), the Green Bank Telescope (GB), Kitt Peak (KP), Los Alamos (LA), Mauna Kea (MK), North Liberty (NL), Onsala (ON), Owens Valley (OV), and Pie Town (PT). 3C 84 was observed in full-track mode for 8 hrs. The data were recorded at an aggregate bitrate of 2 Gbps with 2 bit digitization. Using the polyphase filterbank, the data were channelized in 8 intermediate frequencies (IFs) per polarization, with an IF bandwidth of 32 MHz, yielding a total recording bandwidth of $2 \times 256 \text{ MHz}$. The data were correlated using the DiFX correlator (Deller et al. 2011) at the Max-Planck-Institut für Radioastronomie (MPIfR) in Bonn, Germany. A summary of details of the observations is given in Table 1.

2.1.1. Total intensity calibration and imaging

The post-correlation analysis and calibration of the correlated data were done using standard VLBI fringe-fitting and calibration procedures in AIPS (Greisen 1990; see also Martí-Vidal et al. 2012 for the analysis of GMVA data). In the first step of the phase calibration, delay and phase offsets between the IFs were removed using high SNR fringe detection (so called manual phase-calibration). After the phase alignment across the IFs, the global fringe fitting was performed over the full bandwidth, in order to solve for the delays and rates combining all IFs. We set the signal-to-noise (S/N) threshold to 5. The number of detections was maximized when we used a rather long fringe solution interval of 4 minutes, which was moved forward in time in 1 minute steps. In the next step, we performed the a-priori amplitude calibration using the AIPS task APCAL, using a-priori calibration information provided by each station (system temperatures T_{sys} and elevation dependent gain curves). An opacity correction was performed for stations which did not apply it in the delivered system temperature values. Finally, the cross-hand phase and delay offsets of the reference station were determined and removed using AIPS task RLDLY. The UVFITS data were then exported outside AIPS using the AIPS task SPLIT by frequency-averaging the cross-power spectra.

At 86 GHz, the atmosphere limits the phase coherence. In order to estimate the effect of coherence losses, we fringe fitted the data once again using much shorter fringe solution intervals comparable to the coherence time. For this purpose, we set the fringe solution interval to 10 sec and adopted the same S/N threshold of 5. We also used more narrow fringe search windows for delay and rate ($\pm 10 \text{ ns}$ and $\pm 25 \text{ mHz}$, respectively). The number of detected scans was reduced dramatically due to the short solution interval. For the detected scans, we found that the short 10-second solution interval did not increase the baseline amplitudes significantly, as long as the phases were not averaged over a longer time interval. (e.g., $\lesssim 10\%$ of decoherence amplitude loss with 10 sec time-averaging).

The frequency-averaged (but not yet time-averaged) data were read into the DIFMAP package (Shepherd et al. 1994) for imaging. We flagged outlying visibilities which were caused by known or previously unrecognized antenna problems (such as pointing and/or focus errors, and bad weather). After an initial phase self-calibration using a point-source model, the visibility data were coherently time averaged over 10 seconds. We then imaged the source structure in Stokes I by applying the standard, iterative CLEAN and self-calibration steps (for both phase and amplitude). With careful CLEAN and self-calibrations, our CLEAN model was able to reach the maximum correlated flux density on the shortest uv-spacings (e.g., $\lesssim 200 \text{ M}\lambda$). We however note that the limited accuracy of the a-priori calibration for

¹ We assume ΛCDM cosmology with $H_0 = 71 \text{ km/s/Mpc}$, $\Omega_\Lambda = 0.73$ and $\Omega_M = 0.27$.

Table 1. Summary of the polarimetric VLBI observations of 3C 84 in May 2015.

Stations (1)	Epoch (2)	ν_{obs} (3)	Beam (4)	I_{peak} (5)	S_{tot} (6)	σ_1 (7)	PI_{peak} (8)	P_{tot} (9)	σ_P (10)
	[yy/mm/dd]	[GHz]	[mas, deg]	[Jy/bm]	[Jy]	[mJy/bm]	[mJy/bm]	[mJy]	[mJy/bm]
VLBA(8)									
+GBT+EB+ON	2015/05/16	86.252	0.048 × 0.14 (-16.2)	1.82	12.0	0.53	27.7	42.0	5.03
VLBA(10)	2015/05/11	43.115	0.15 × 0.30 (1.02)	3.82	17.0	1.24	12.3	16.8	1.75
VLBA(10)	2015/05/18	15.352	0.42 × 0.63 (-8.74)	4.00	28.8	1.30	< 2.64	–	0.88

Notes. (1) Antennas participating in each epoch. Numbers in the bracket indicates the number of the VLBA antennas participated. (2) The observing epoch in year/month/day format. (3) Center frequency. (4) The restoring beam for the uniform weighting. Minor axis × major axis in mas (the position angle in degrees measured counterclockwise from North). (5) Total intensity peak (in units of Jy per beam). (6) Total flux density integrated over the entire VLBI image. (7) Total intensity rms level. (8) Linear polarization intensity peak (upper limit for 3σ significance). (9) Integrated linearly polarized flux density of the core region obtained by the quadratic sum of the integrated Stokes Q and U flux densities in the region where significant linear polarization intensities are found (“–” means no significant linear polarization in the region displayed in Fig. 2 and 3). (10) The polarization intensity noise level obtained as described in Sect. 2.1.3.

the stations which form the shortest baselines (e.g., PT and LA) could have an effect on the maximum absolute flux density.

In order to correct for a systematic flux density scaling, we combined quasi-simultaneous data from VLBA observations of the source at 15 and 43 GHz (Sect. 2.2) and computed the synchrotron spectrum of the extended jet in the source (at ~ 2 – 4 mas from the VLBI core). We then assumed that the observed spectral index of the extended jet components between 15 and 43 GHz is constant (no spectral break), and thus is the same as at the higher frequencies (i.e., between 43 and 86 GHz). Based on this assumption and the observed spectral index of $\alpha_{15-43 \text{ GHz}} \sim -0.5$ ($S \propto \nu^{\alpha}$), we estimated a correction factor for the absolute flux density of the source and further calibrated the data. We also checked the accuracy of the absolute flux density by making use of close-in-time single-dish observations and connected interferometer flux measurements of the source between 15 and 343.5 GHz. From this we conclude that the absolute flux density of the source in this epoch could be uncertain by $\sim 30\%$ (see Appendix A for details).

We examined the reliability of the CLEAN model and the self-calibration solutions by comparing the closure phases and amplitudes of the a-priori calibrated data and the CLEAN model. In particular, we compared the differences (and ratios) of the closure phases (and closure amplitudes) between the data and the model. The residual closure phases and the closure amplitudes ratios were computed for the histograms of the entire data. We found that the closure quantities of the a-priori calibrated data and the CLEAN model agreed within $\sim 10^\circ$ for the phases and $\sim 25\%$ for the amplitude, respectively.

A summary of characteristics of the final 86 GHz Stokes I image is given in Table 1. In Fig. 1 we show the (u, v) coverage of the data set and the visibility amplitudes versus the (u, v) -distances after all the calibrations.

2.1.2. Polarization calibration and imaging

After the total intensity imaging, additional calibration steps were performed in AIPS in order to remove residual gain offsets between the RCP and LCP receivers and the polarization leakage effects. In particular, the antenna instrumental polarization solutions (D-terms) were determined using the AIPS task LPPCAL (Leppanen et al. 1995). We derived the D-terms from other more compact calibrator sources including 3C 454.3, BL Lac, CTA 102, and OJ 287, which were observed in the same session. We also derived the D-terms from 3C 84 itself, which is facilitated by (i) its core-dominance at millimeter wavelengths (see

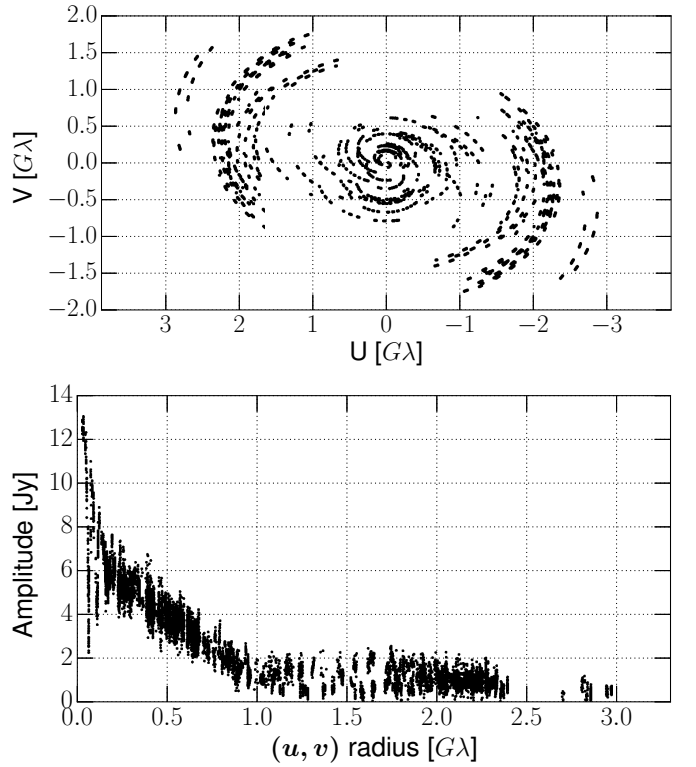


Fig. 1. Stokes I visibilities of the GMVA data. *Top*: The (u, v) -coverage after the a-priori calibration and additional flagging for the imaging. *Bottom*: Radial distribution of the visibility amplitudes after the last round of CLEAN and self-calibration. The visibility data were binned in 30 sec for clarity.

Sect. 3) and (ii) wide parallactic angle coverage in this data set. We show two linear polarization images of 3C 84 in Appendix B for D-terms solutions derived from CTA 102 and OJ 287. The maps show a broadly consistent appearance of the polarization. In order to obtain a final set of D-terms, we vector-averaged the D-terms and created the final polarization image of 3C 84 for further analysis. Confidence in the final D-terms was obtained by imaging the polarized structure of the calibrators. Their GMVA polarization images showed good agreements with contemporaneous VLBA 43 GHz polarization images available from the VLBA-BU-BLAZAR database², but with more fine-scale struc-

² <https://www.bu.edu/blazars/VLBAproject.html>

ture seen in the GMVA images. Those images will be published later elsewhere.

The final D-term solutions are tabulated in Table 2. Their errors are estimated based on the standard deviation of the different D-term values for each station and polarization.

The absolute electric vector position angle (EVPA) of 3C 84 was calibrated using OJ 287, 3C 454.3, and BL Lac. These calibrators were also observed as part of the POLAMI (Polarimetric Monitoring of AGN at Millimeter Wavelengths) program³ (Agudo et al. 2018a) by the IRAM 30m Telescope, which was equipped with the XPOL polarimeter (Thum et al. 2008). We estimate the overall uncertainty of the EVPA measurements in GMVA data using the following procedure: first, the measurement error of the 86 GHz EVPA in the IRAM 30m Telescope data is $\sim 2 - 7$ deg for different sources and for this particular epoch (see also Agudo et al. 2018a). By deriving the VLBI EVPA correction values from multiple calibrators, we adopt a conservative absolute EVPA uncertainty of ~ 10 deg. Second, the polarization angle of the source and the D-term phases are correlated and uncertainties of the latter could affect the accuracy of the former (see, e.g., Eq. 3 and 13 of Leppanen et al. 1995). The average phase errors of the D-terms is ~ 24 deg (Table 2). Accordingly, we estimate that the corresponding EVPA uncertainty would be $\sim 24/2 = 12$ deg. Third, we compute the peak-to-noise of the polarization features in Stokes Q and U and propagate the errors to estimate the EVPA uncertainty due to the thermal noise. Under the assumption that these three measurements errors are uncorrelated, we can add them in quadrature. For a signal-to-noise of ~ 5 , this leads to the overall EVPA uncertainty of ~ 17 deg in this GMVA observation.

2.1.3. Estimating noise levels in the polarization image

The Rice bias correction for polarization measurements (see, e.g., Wardle & Kronberg 1974; Montier et al. 2015a,b) requires an accurate estimation of the signal-to-noise ratio. We simulated the probability density distribution of the noise in the linear polarization intensity image, σ_P , by performing a Monte-Carlo simulation. First, we computed the 1σ noise levels for Stokes Q and U by fitting Gaussian functions to pixel value histograms of source-free regions in the Stokes Q and U images. We then simulated Gaussian-distributed noises for Q and U and added them in quadrature to obtain the probability distribution of the polarization noise. By calculating the 68%, 97%, and the 99.7% confidence levels, we obtained the noise values of 5.7, 9.5, and 14.0 mJy/beam for the conventional 1σ , 2σ , and 3σ levels, respectively. Based on this, we adopt $1\sigma_P \sim 5$ mJy/beam at 86 GHz.

We note that this value is higher than the noise in the Stokes I image ($\sigma_I \sim 0.5$ mJy/beam). In the ideal case, the noise level of a linear polarization map, σ_P , is expected to be comparable to or lower than that of the total intensity map, σ_I , because the latter is often dynamic-range limited (see, e.g., Thompson et al. 2017). However, this is not the case if systematic polarization calibration errors dominate the polarization noise (e.g., due to errors in the D-terms). Thus, we checked if the increased noise level in the linear polarization map could be due to uncertain D-term solutions. Following Roberts et al. (1994) (see also Hovatta et al. 2012), we estimate the error from D-term calibration as follows:

$$\sigma_{\text{Dterm}} = \frac{\Delta m}{\sqrt{N_{\text{ant}} \times N_{\text{IF}} \times N_{\text{scan}}}} \sqrt{I^2 + (0.3 \times I_{\text{peak}})^2} \quad (1)$$

³ <http://polami.iaa.es/>

Table 2. Summary of the antenna D-terms at 86 GHz. The Green Bank Telescope was used as the reference antenna. The columns show (1) the station code, (2,3) the amplitude (m) and phase (χ) of the D-terms for the RCP, and (4,5) the same for the LCP.

Station (1)	RCP		LCP	
	m [%] (2)	χ [deg] (3)	m [%] (4)	χ [deg] (5)
BR	5.8 ± 2.7	$-(106 \pm 16)$	7.2 ± 2.7	$-(48 \pm 20)$
EB	4.5 ± 2.1	56 ± 24	2.3 ± 2.5^a	98 ± 40^a
FD	7.9 ± 2.9	23 ± 13	7.0 ± 3.6	$-(141 \pm 25)$
GB	1.7 ± 2.4^a	$-(162 \pm 46)^a$	2.6 ± 1.3	$-(66 \pm 44)^a$
KP	3.1 ± 2.8	178 ± 30	3.8 ± 1.7	88 ± 14
LA	10.7 ± 1.6	139 ± 9	10.1 ± 2.1	32 ± 13
MK	3.9 ± 3.1	11 ± 25	4.3 ± 1.9	$-(90 \pm 23)$
NL	4.8 ± 1.6	$-(167 \pm 21)$	3.7 ± 1.3	70 ± 13
ON	5.9 ± 1.9	$-(178 \pm 27)$	4.8 ± 2.4	$-(4 \pm 36)$
OV	3.6 ± 2.4	$-(48 \pm 38)$	5.4 ± 1.7	$-(127 \pm 21)$
PT	8.2 ± 5.6	7 ± 8	9.6 ± 3.4	$-(134 \pm 21)$

Notes. ^(a) Small D-term amplitudes induce large uncertainties in the D-term phases.

where Δm is the error of the D-term amplitudes, N_{ant} is the number of the antennas, N_{IF} is the number of IFs, N_{scan} is the total number of independent scans with different parallactic angles, I is the total intensity pixel values, and I_{peak} is the peak value of the total intensity image. As shown in Table 2, the D-term amplitudes are uncertain by $\sim 2 - 4\%$ (the largest uncertainty of $\sim 5\%$ is found for RCP at PT). Therefore, we assume that a characteristic value of Δm is ~ 0.03 . For the GMVA data of 3C 84, we adopt $N_{\text{ant}} = 11$ and $N_{\text{IF}} = 8$. The number of independent scans including all the antennas was $N_{\text{scan}} = 8$. This gives us a characteristic $\sigma_{\text{Dterm}} \sim 10^{-3} \times I_{\text{peak}}$. For $I_{\text{peak}} = 1.8$ Jy/beam, we obtain $\sigma_{\text{Dterm}} \sim 2$ mJy/beam. The order of σ_{Dterm} appears to be in agreement with our estimation of σ_P , suggesting that residual polarization leakages may dominate the polarization noise in our 86 GHz image.

2.2. Contemporaneous 43 and 15 GHz VLBA data

On short timescales of \lesssim one week, the structural variability of 3C 84 is likely negligible because of the known slow apparent jet speed of $0.1c \sim 0.1$ mas/yr $= 2\mu\text{as/week}$ in the core region of 3C 84 (Walker et al. 1994; Suzuki et al. 2012). This allows to combine the 86 GHz data with quasi-contemporaneous observations at other frequencies.

We made use of archival polarimetric VLBA data of 3C 84 provided by the MOJAVE program⁴ (15 GHz; Lister & Homan 2005) and the VLBA-BU-BLAZAR monitoring program (43 GHz; Jorstad et al. 2017). We have chosen a set of 15 GHz and 43 GHz data which were obtained closest in time to the GMVA observations. The archival data were observed with the same dual polarization setup (RCP and LCP) and the same total bandwidth of 2×256 MHz. The Stokes I , Q , and U maps again were obtained using DIFMAP, averaging the visibilities over the whole observing bandwidth. At these two frequencies, we estimate the polarization image noise levels σ_P in the same way as described in Sect. 2.1.3. The σ_P values were comparable to σ_I , indicating that at these lower frequencies the systematic uncer-

⁴ <https://www.physics.purdue.edu/MOJAVE/>

tainties in the linear polarization due to errors in the D-terms are small. A summary of the two data sets is given in Table 1.

For the absolute EVPA measurement error (i.e., those arising from the D-term calibration and absolute EVPA correction), we adopted 5 deg and 10 deg at 15 GHz and 43 GHz based on Lister & Homan (2005) and Jorstad et al. (2005), respectively. The overall uncertainty for the EVPA was then estimated in the same way as we described in Sect. 2.1.2 by adding the systematic and thermal errors in quadrature.

In addition, the VLBA-BU-BLAZAR program provides the VLBA 43 GHz data at four different frequencies in the 43 GHz band (43.0075, 43.0875, 43.1515, and 43.2155 GHz). Their polarization calibration has been performed separately for each IF with respect to the D-terms and EVPA values (see Sect. 3.1 of Jorstad et al. 2005). Therefore, we created additional 43 GHz polarization images of the source for each of the four IFs separately, in order to resolve the $n\pi$ angle ambiguity in the rotation measure analysis and to check for a possible large EVPA rotation inside the 43 GHz band.

2.3. Non-contemporaneous VLBA data at 43 GHz

We also analyzed other VLBA 43 GHz data of 3C 84 available from the BU database in order to study the time variability of the total flux and the linear polarization over a longer period. We specifically focused on observations performed in 2015 (eight epochs; Feb, Apr, May, Jun, Jul, Aug, Sep, and Dec). We imaged the source again by applying some additional data flagging when systematically large errors were clearly seen in some antennas or scans. The full-polarization images available from the BU database reveal a weak polarization feature in the core region of 3C 84 in all the eight epochs during 2015. In our imaging, we recover a very similar polarization morphology in most epochs, however some epochs (Feb, Jun, Aug, and Dec) appear to be more limited in polarization fidelity, possibly due to the limited number of scans or other systematic errors. Therefore, we did not include these polarization images in our analysis. Overall, repeatedly appearing and therefore reliable polarization features have been detected in four (Apr, May, Jul, and Sep) out of the eight epochs. We also measured the unpolarized core flux for all the eight epochs using the MODELFIT routine implemented in DIFMAP and analyzed their uncertainties following Schinzel et al. (2012) (see Sect. 2.5). We summarize details for these data in Appendix C.

2.4. Contemporaneous ALMA data

Finally, we made use of contemporaneous (May 2015) linear polarization measurements of 3C 84 from the Atacama Large Millimeter/submillimeter Array (ALMA) Calibrator Source Catalogue⁵. The source was observed at 97.5, 233.0, and 343.5 GHz and was not resolved up to the baseline length of $537.5 k\lambda$ at all frequencies. Therefore, we constrain the source size to be $< 1/(537.5 \times 10^3) \text{ rad} \approx 0.38 \text{ arc second}$. Table 3 summarizes the archival ALMA polarization measurements.

2.5. Model-fitting, polarization measurements, and their uncertainties

In order to parameterize the size and the flux density of the VLBI core region in Stokes I , we made use of the MODELFIT procedure implemented in DIFMAP. We fitted circular Gaussians to

Table 3. Summary of the ALMA archival data. The columns show (1) the observing epoch, (2) the central frequency, (3) the total flux, (4) the degree of the linear polarization, and (5) the EVPA.

Epoch (1) [yyyy/mm/dd]	ν_{obs} (2) [GHz]	S_{tot} (3) [Jy]	m_L (4) [%]	EVPA (5) [deg]
2015/05/31	97.5	17.14 ± 0.57	0.6 ± 0.3	82.1 ± 19.7
	233.0	9.82 ± 0.33	1.0 ± 0.3	$-(29.1 \pm 12.1)$
	343.5	6.85 ± 0.23	0.3 ± 0.3	18.3 ± 42.9

the visibilities at each frequency and estimated their uncertainties following Schinzel et al. (2012). For the absolute flux density at 86 GHz, we conservatively adopt an uncertainty of $\sim 30\%$ based on the limitation of the absolute flux calibration in this epoch.

The polarization components were identified by the local maxima of their linearly polarized intensities in the image plane (see Fig. 3 and 7). For each component, we define a circular aperture whose diameter matches the mean beam size and is centered at the local peak of the polarized intensity. The properties of the polarized components – i.e., the Stokes I flux density S , the linearly polarized flux density P , the degree of linear polarization m_L , and the EVPA χ – were then determined from the spatially integrated Stokes I , Q , and U flux densities. Specifically, the integrated flux densities and the polarization parameters were computed by

$$Q_{\text{tot}} = \sum Q_{i,j} \times A_{\text{pixel}}/A_{\text{Beam}} \quad (\text{in Jy}) \quad (2)$$

$$U_{\text{tot}} = \sum U_{i,j} \times A_{\text{pixel}}/A_{\text{Beam}} \quad (\text{in Jy}) \quad (3)$$

$$S = \sum I_{i,j} \times A_{\text{pixel}}/A_{\text{Beam}} \quad (\text{in Jy}) \quad (4)$$

$$P = \sqrt{Q_{\text{tot}}^2 + U_{\text{tot}}^2} \quad (\text{in Jy}) \quad (5)$$

$$m_L = 100 \times P/S \quad (\text{in percent}) \quad (6)$$

$$\chi = 0.5 \arctan(U_{\text{tot}}/Q_{\text{tot}}) \quad (\text{in radian}) \quad (7)$$

where $I_{i,j}$, $Q_{i,j}$ and $U_{i,j}$ are the corresponding Stokes intensity values at each pixel (i, j) in Jy/beam and A_{pixel} and A_{Beam} are the pixel and the beam area in square mas, respectively⁶. In these calculations, we also corrected for the Rice bias in the polarization intensity value at each pixel by following Wardle & Kronberg (1974). We assume that the uncertainty of P is 30% at all frequencies. For S , we assume 10% uncertainties at ≤ 43 GHz (e.g., Lister & Homan 2005; Jorstad et al. 2005) but 30% at 86 GHz as explained before. The uncertainty of m_L was then obtained by propagating the errors of the integrated flux densities. The EVPA error was calculated as described in Sect. 2.1.2.

3. Results

3.1. Total intensity structure and the core flux

In Fig. 2 we show the quasi-simultaneous polarimetric VLBI images of 3C 84 at 15 GHz and 43 GHz in May 2015. The GMVA 86 GHz images are shown in Fig. 3 with two different restoring beams in order to better illustrate both the extended and inner jet

⁶ We compute the area under the elliptical Gaussian beam, A_{Beam} , by $A_{\text{Beam}} = \pi \psi_{\text{maj}} \psi_{\text{min}} / 4 \ln 2$ where $\psi_{\text{maj,min}}$ are the FWHM of the elliptical Gaussian along the major and the minor axis, respectively. The areas of individual pixels, A_{pixel} , are 0.01×0.01 , 0.02×0.02 , and 0.03×0.03 square mas at 86, 43, and 15 GHz, respectively.

⁵ <https://almascience.eso.org/alma-data/calibrator-catalogue>

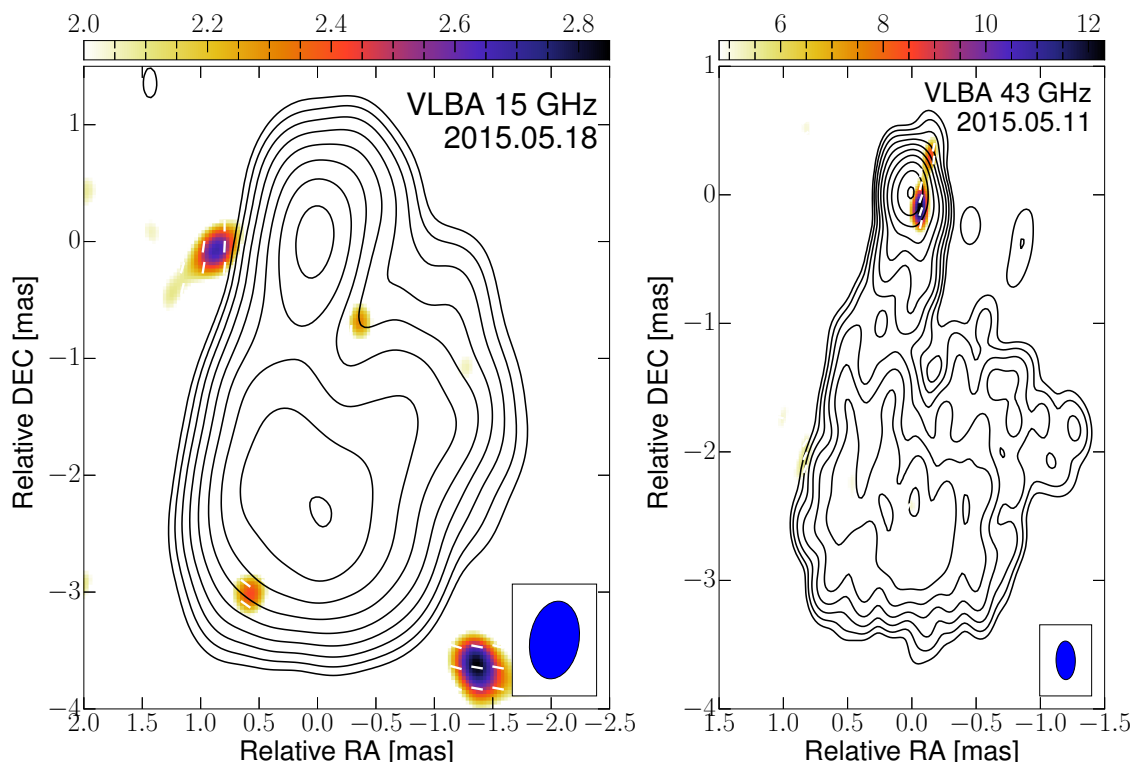


Fig. 2. Polarimetric VLBI images of 3C 84 at 15 and 43 GHz. In both panels, the contours show the total intensity and increase by a factor of 2 from the lowest level. The color scale represents the polarized intensity (in mJy/beam). The white bars in the images display the apparent EVPA. The blue ellipse in the bottom right corner shows the restoring beam. *Left* : VLBA 15 GHz image. The contours start at 30 mJy/beam. The color scale starts at 2.0 mJy/beam. *Right* : VLBA 43 GHz image. The contours start at 7 mJy/beam. The color scale starts at 4.8 mJy/beam.

structure. The source clearly shows a limb-brightened jet at high frequencies (≥ 43 GHz). The limb-brightening is visible up to ~ 2 mas from the core. We made transverse cuts to the jet at a core separation $z \sim 0.4$ mas at 43 GHz and 86 GHz using the full-resolution image (Fig. 3, right) and show the intensity profiles of the slices in Fig. 4. The limb-brightened transverse structure is consistent with previous deep single-epoch (Nagai et al. 2014) and long-term (Jorstad et al. 2017) VLBA 43 GHz observations of the source. At 86 GHz, the improved angular resolution resolves the edge-brightened structure down to ~ 0.2 mas core distance. Remarkably, within the inner 0.2 mas from the intensity peak, the nuclear region appears substantially resolved in the E-W direction and shows a complex morphology. The 86 GHz core is well represented by a single circular Gaussian component whose FWHM size is comparable to the 43 GHz core. However, the visibilities at long baselines ($\sim 1.0 - 2.5 G\lambda$) suggest the presence of a more complex sub-nuclear structure (see Fig. 1). On larger scales, the overall source structure is quite similar to that shown in the 43 GHz image (cf. Fig 2 and 3), but the extended jet emission at larger core separations is overall fainter. A more detailed study of the total intensity structure is beyond the focus of this paper and will be presented elsewhere.

In Table 4 we show the flux densities S_{mod} and FWHM sizes of the core at 15, 43 and 86 GHz obtained with the MODELFIT procedure of DIFMAP. We fitted a single power-law to the core spectrum, i.e. $S \propto \nu^{\alpha}$ where ν is the observing frequency and α is the spectral index. The results are shown in the left panel of Fig. 5. We find that the spectrum of the VLBI core is slightly inverted up to 86 GHz with a spectral index of $\alpha = 0.51 \pm 0.10$. We also show the time variation of the core flux at 43 GHz in Fig. 6. In the same figure we also provide the peak values obtained with a circular Gaussian beam of 0.3 mas. The core brightens by

~ 2 Jy during 2015 and reaches a local maximum during June and July 2015.

3.2. Linear polarization in the core region

In Fig. 7 we show the linear polarization structure in the core region at 43 and 86 GHz in more detail, restoring the maps with the VLBA 43 GHz beam at both frequencies for better comparison. In May 2015, we detect linear polarization features in the core at high significance ($PI_{\text{peak}}/\sigma_P \sim 7.0$ and 5.5 at 43 and 86 GHz, respectively; see Table 1). At 15 GHz, no significant polarization features appear in the nuclear region. The polarization features at both 43 and 86 GHz are slightly offset from the peak of the total intensity. The features P1 and P2 (i.e., P2a+P2b) are separated by ~ 0.2 mas in the east-west orientation, and could possibly be associated with the edges of the underlying limb-brightened jet seen at 22 GHz by recent RadioAstron observations (e.g., Giovannini et al. 2018). The P2 component is present in both maps at similar locations. However, the P1 component in the 86 GHz image has no clear counter-part at 43 GHz. Using the pixel values at the position of P1, we estimate a $3\sigma_P$ upper limit of m_L of P1 is $\lesssim 0.2\%$ at 43 GHz. At 43 GHz, there exists another polarized feature (~ 8 mJy/beam) at a separation of ~ 0.3 mas to the north of the core, perhaps associated with a counter-jet. We searched the VLBA-BU-BLAZAR database for evidence in support of significant polarization north to the main intensity peak in several epochs. While the polarization detection close to the total intensity peak can be seen in many epochs, we found polarization north of it only in a few epochs. Therefore we do not find strong evidence for a persistent polarization on the counter-jet side. Except for this faint northern polarization fea-

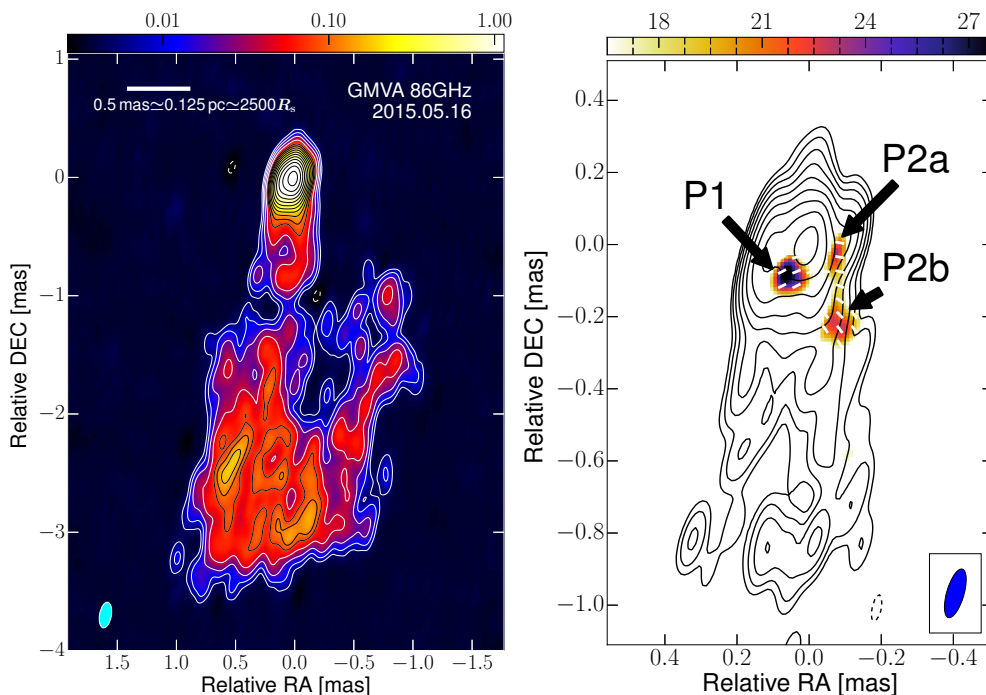


Fig. 3. GMVA 86 GHz images of 3C 84. In both panels, the contours show the total intensity and increase by a factor of 2 from the lowest level (5 mJy/beam). A negative contour of -5 mJy/beam is also shown with dashed lines. *Left* : The Stokes I image restored with an elliptical beam of 0.22×0.10 mas and position angle of -10° . This beam is larger than the full resolution attainable with the GMVA. The peak of this image is 3.04 Jy/beam. The cyan ellipse in the left bottom corner illustrates the elliptical beam. The color scale represents the Stokes I pixel values in Jy/beam. The white bar and the text in the upper left corner denote the projected spatial scale of the image. *Right* : The inner jet structure obtained with the full angular resolution of the GMVA. The color scale represents the linear polarization intensity and starts from 16.5 mJy/beam.

ture, the 43 GHz VLBA polarization images in the other epochs show similar linear polarization flux densities in the core region, although the relative position of the polarization peak seem to change with time (see Appendix C).

At 86 GHz, the degrees of the linear polarization m_L of the polarized components are in the range of $\sim 3 - 6\%$ when convolved with the small GMVA observing beam. The 86 GHz m_L values decrease to $\sim 1 - 2\%$ when convolved with the VLBA 43 GHz beam. For the P2 component, the m_L value is significantly lower at 43 GHz ($\sim 0.4 - 0.5\%$ in this epoch). At 15 GHz, the non-detection suggests a 3σ upper limit to m_L of $\lesssim 0.1\%$, which is in agreement with the results of Taylor et al. (2006). In order to minimize the effect of the different angular resolutions of the VLBA and the GMVA images, we now determine the polarization properties convolving the maps with the same VLBA 43 GHz beam (Fig. 7) and compare the results in the following analysis. Table 5 provides a summary of the properties of the polarized components in May 2015 (see Appendix C for results at 43 GHz at other epochs).

In order to investigate the frequency dependence of the linear polarization of the core region, we combined linear polarization measurements from the literature with the data from this paper. The results are shown in the right panel of Fig. 5. The linear polarization of the core clearly shows an increasing trend with frequency, which can be represented by a power-law fit $m_L \propto \nu^{0.77 \pm 0.18}$, in which we have combined all available m_L measurements. We note that the index of the power-law could be affected by some systematic uncertainties due to the different angular resolutions of the telescopes. Nevertheless, we can clearly see that both VLBI and non-VLBI measurements show an increase of linear polarization degree towards higher frequencies.

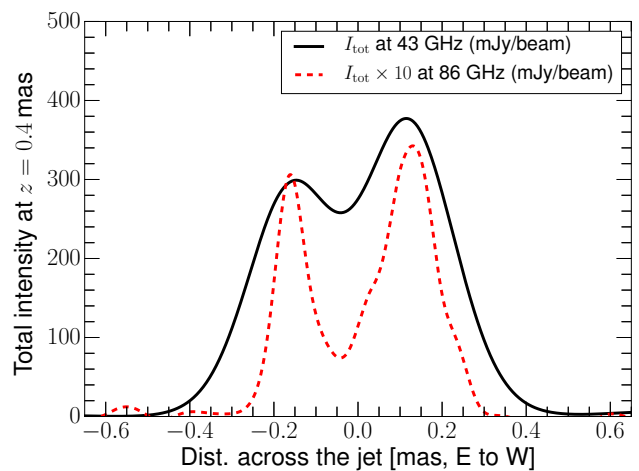


Fig. 4. Transverse jet intensity profiles at 43 GHz (black solid line) and 86 GHz (red broken line) obtained at 0.4 mas core distance as function of distance across the jet (increasing towards west).

Table 4. VLBI core properties in May 2015. The columns show (1) the central observing frequency and (2,3) the total flux and the FWHM size of the VLBI component obtained by the Gaussian model-fitting.

ν_{obs} (1) [GHz]	S_{mod} (2) [Jy]	FWHM (3) [mas]
86	5.6 ± 1.7	0.13 ± 0.04
43	4.8 ± 0.7	0.14 ± 0.01
15	2.6 ± 0.4	0.27 ± 0.02

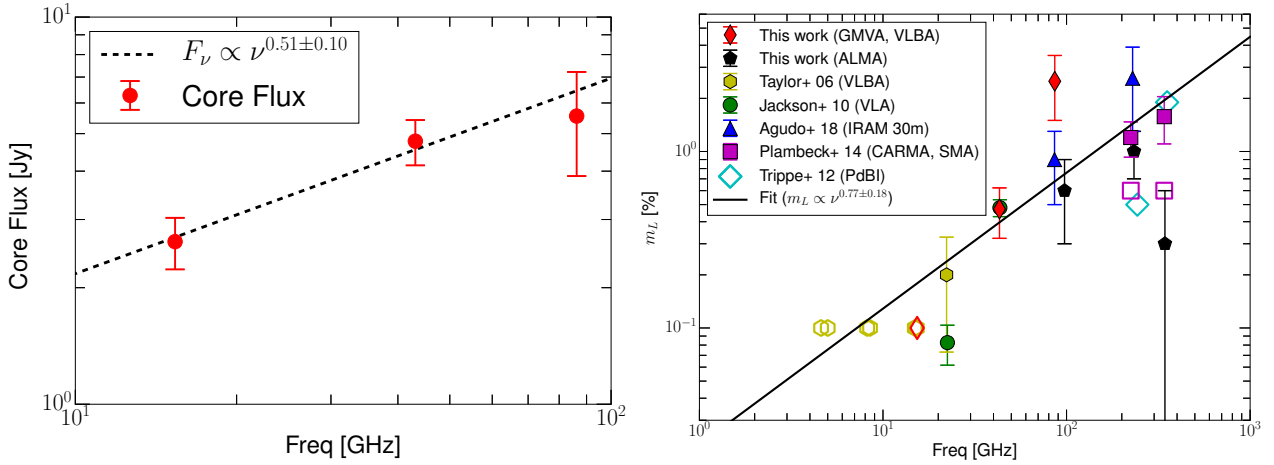


Fig. 5. *Left* : Total intensity spectrum of the VLBI core region between 15 and 86 GHz. *Right* : The degree of linear polarization in the VLBI core region obtained from this work and previous VLBA observations (Taylor et al. 2006) and integrated values from the literature (Jackson et al. 2010; Trippe et al. 2012; Plambeck et al. 2014; Agudo et al. 2018b). All the VLBI polarization measurements were made from the pixel values near the peak of the Stokes I . Filled and open symbols of the same marker indicate measured values and upper limits, respectively. Citations and corresponding instruments are shown in the legend. We note that at 230 GHz only upper limits were observed before May 2011 (Trippe et al. 2012; Plambeck et al. 2014). After October 2011, Plambeck et al. (2014) report a significantly higher linear polarization degree.

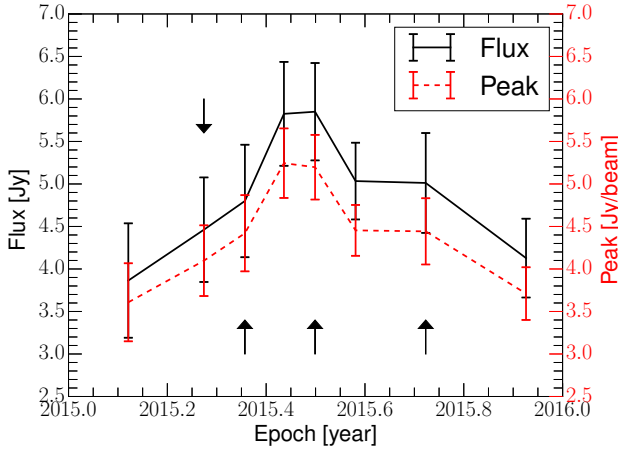


Fig. 6. VLBA 43 GHz core flux and the peak values during 2015. Arrows indicate epochs when reliable polarization has been detected.

3.3. Rotation measure between 43 GHz and 344 GHz in May 2015

We determine the rotation measure (RM) associated with the Faraday rotation by measuring the variation of the observed EVPA with frequency. When a linearly polarized wave at a wavelength λ passes through magnetized plasma, the intrinsic EVPA of the emission χ_{int} is rotated and the observed EVPA $\chi(\lambda)$ is

$$\chi(\lambda) = \chi_{\text{int}} + \text{RM} \times \lambda^2 \quad (8)$$

The rotation measure RM is determined by the gradient of $\chi(\lambda)$ versus λ^2 after solving for the $n\pi$ ambiguity in the angle. To resolve the $n\pi$ ambiguity, we assume that most of the polarized flux observed by the ALMA at 97.5, 233.0, and 343.5 GHz originates from the same VLBI core region. This assumption appears to be reasonable based on the flat spectrum of the linearly polarized flux density between 97.5 and 233.0 GHz measured by ALMA (~ 100 mJy at both frequencies; see Table 3). Next, we compute the integrated Stokes Q and U flux densities of the VLBI core region at 43 and 86 GHz to obtain the spatially integrated EVPAs. The spatially integrated EVPAs within the 43 GHz band are shown in Table 5. At 86 GHz, the integrated EVPA is $\chi = -(70 \pm 16)$ deg. Then we compare all these EVPAs simultaneously to find a best λ^2 fit.

We resolve the $n\pi$ ambiguity by following Hovatta et al. (2012). The authors determined the smallest possible EVPA rotations at each frequencies to achieve a statistically acceptable fit with the λ^2 model. Similarly, we rotated the 86.0, 97.5, 233.0, and 343.5 GHz EVPAs by $(n_1, n_2, n_3, n_4) \times \pi$ respectively where $n_i \in (-30, -29, \dots, 29, 30)$ and $i \in (1, 2, 3, 4)$. Then we calculated corresponding χ^2 values for each rotation. We note that $n = 30$ corresponds to $\text{RM} \sim 10^8$ rad/m² for the frequency range considered here. $\text{RM} \sim 10^8$ rad/m² is also equivalent to a single 180° wrap within the 43 GHz band. Therefore, we are assuming that there is no $\text{RM} \gtrsim 10^8$ rad/m² in the source (cf. Plambeck et al. 2014). For the same reason, we did not apply the $n\pi$ rotation within the 43 GHz band. Then we chose a set of n_i which provided minimum χ^2 value.

We find a best λ^2 fit with $n_1 = -2$, $n_2 = -3$, $n_3 = -3$, and $n_4 = -3$ (corresponding $\chi^2 = 3.52$ and the reduced $\chi^2 =$

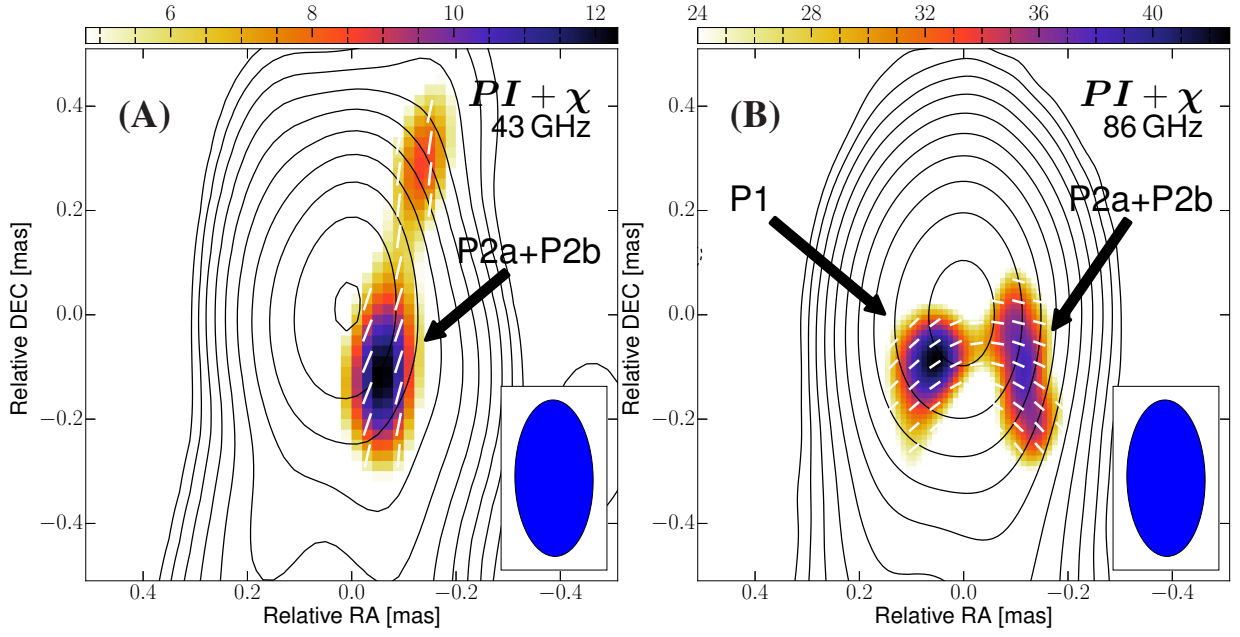


Fig. 7. Comparison of the total intensity, the polarized intensity (PI), and the polarization angle (χ) in the nuclear region at 43 and 86 GHz. The maps are restored with the same VLBA 43 GHz CLEAN beam and displayed over the same RA and DEC ranges (± 0.5 mas). The arrows show the polarized component identifications. (A) : The same as the central panel of Fig. 2 (43 GHz) but zoomed in the core. (B) : GMVA 86 GHz total and linear polarization image restored with the VLBA 43 GHz beam. The contours start at 6 mJy/beam and increase by a factor of 2 from the lowest level. The color scale starts from 24 mJy/beam.

Table 5. Properties of the polarized components in May 2015. The columns show (1) the central frequency, (2) the component identification, (3) the Stokes I flux density, (4) the degree of linear polarization, and (5) the EVPA. The Stokes I flux densities are consistent at the four separate frequencies within the 43 GHz band and we omit the numbers for the other three 43 GHz sub-bands.

ν_{obs} (1) [GHz]	ID (2)	S_ν (3) [Jy]	m_ν (4) [%]	χ_ν (5) [deg]
86.252	P1	0.70 ± 0.21	3.4 ± 1.4	$-(54 \pm 17)$
	P1 ^a	1.5 ± 0.4	1.4 ± 0.6	$-(43 \pm 17)$
	P2a	0.27 ± 0.08	6.3 ± 2.7	$-(89 \pm 17)$
	P2b	0.05 ± 0.02	44 ± 20^b	47 ± 17^b
	P2a+P2b ^a	1.3 ± 0.4	2.2 ± 0.9	71 ± 17
43.0075	P2a+P2b	2.0 ± 0.2	0.44 ± 0.14	$-(9 \pm 10)$
43.0875			0.49 ± 0.16	$-(20 \pm 10)$
43.1515			0.53 ± 0.17	$-(24 \pm 10)$
43.2155			0.43 ± 0.13	$-(15 \pm 10)$
15.352		N/A	$< 0.1^c$	N/A

Notes. ^(a) Obtained from the image in panel (B) of Fig. 7. ^(b) The component is associated with the outer edge of the jet and could have higher systematic uncertainties than our estimation. ^(c) 3σ upper limit from the non-detection.

0.59; see Fig. 8). Accordingly, we obtain $RM = (2.02 \pm 0.03) \times 10^5 \text{ rad/m}^2$ and $\chi_{\text{int}} = -(578 \pm 7) \text{ deg}$ (or equivalently $\chi_{\text{int}} = -(38 \pm 7) \text{ deg}$). We note this RM is comparable to $RM \sim 9 \times 10^5 \text{ rad/m}^2$ previously reported by Plambeck et al. (2014).

3.4. Rotation measure within the 43 GHz band

We applied the same RM fitting procedure to the multi-epoch VLBA 43 GHz data using the EVPAs measured at the four different IFs. We tested the significance of the EVPA rotation within

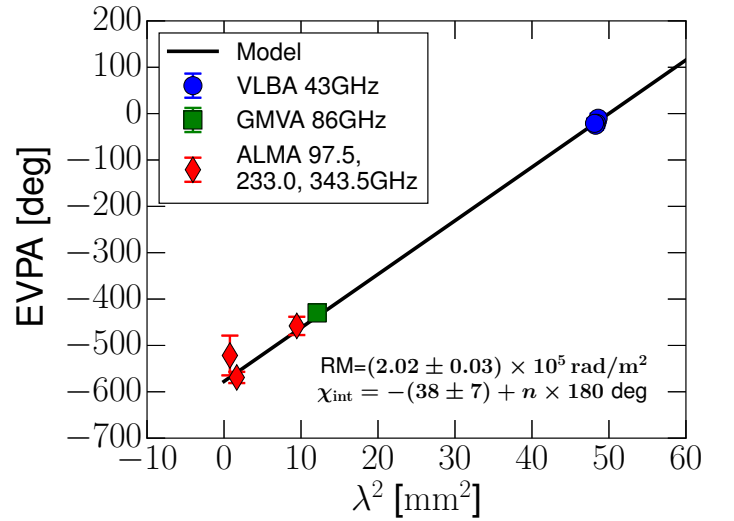


Fig. 8. Spatially integrated EVPA versus the squared wavelength λ^2 (error bars) and the best λ^2 fit (solid line) in May 2015.

the 43 GHz band for 3C 84 by performing the same analysis to the core regions of two comparison sources 0235+164 and 3C 279, which were observed in the same epochs by the VLBA-BU-BLAZAR monitoring program. The instrumental polarization calibration and the sub-band EVPA calibration for the two sources were completely identical to those of 3C 84 during 2015. Therefore, we expect that the EVPA change within the 43 GHz band will be systematically the same for the three sources if the EVPA changes are dominated by residual calibration errors.

In Fig. 9 we show the EVPAs χ for 0235+164 and 3C 279, with respect to their mean values, $\langle \chi \rangle$. Within the 43 GHz band, the EVPA of 3C 279 varies only by ≤ 6 deg in all epochs (≤ 8 deg for 0235+164). This is insignificant compared to our presumed

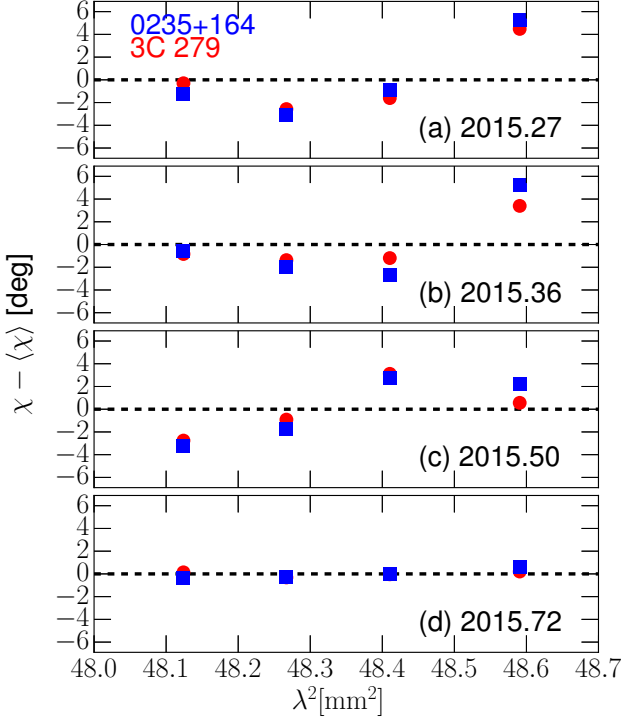


Fig. 9. Variation of the EVPA in each sub-band, χ , with respect to the mean EVPA, $\langle\chi\rangle$. Blue squares and red circles are for 0235+164 and 3C 279, respectively. Error bars are omitted for clarity. Note the strong correlation between the two sources.

Table 6. RM within the VLBA 43 GHz band. From left to right, columns denote the observing epoch, the RM, and the EVPA interpolated to the central frequency of the 43 GHz band (43.1155 GHz).

Epoch [yyyy/mm/dd]	RM [$\times 10^5$ rad/m ²]	χ [deg]
2015/04/12	$-(6.2 \pm 2.6)$	11 ± 5
2015/05/11	2.7 ± 3.5	$-(14 \pm 5)$
2015/07/02	6.8 ± 3.3	$-(11 \pm 5)$
2015/09/22	5.2 ± 4.2	$-(8 \pm 5)$

10 deg angle uncertainty at 43 GHz. In addition, the two sources show strongly correlated EVPA offset from their mean values in all epochs. From this we determine that the 43GHz in-band RM values smaller than $\sim (2 - 3) \times 10^5$ rad/m² are insignificant against the residual calibration errors.

After this consideration, we show the EVPAs measured from the core of 3C 84 at 43 GHz band in Fig. 10. The corresponding RM values obtained from the fitting are tabulated in Table 6 and a plot of the RM versus time is given in Fig. 11. In contrast to 0235+164 and 3C 279, 3C 84 shows much larger EVPA variation within the 43 GHz band (15 – 21 deg). These EVPA variation with wavelength is larger than the residual calibration errors that we estimated. This results in a significant RM ($|RM| \gtrsim 5 \times 10^5$ rad/m² for three out of four epochs). Accordingly, we consider the large RM obtained for 3C 84 within the 43 GHz band is intrinsic to the source. We also note a discrepancy in the form of a negative RM (i.e., decreasing EVPA value with increasing λ^2), which is present only in Apr 2015. We note that the EVPAs of the calibrators in this epoch generally increase with increasing λ^2 (see the top panel of Fig. 9). If the systematic EVPA rotation in the calibrators would be purely due to residual

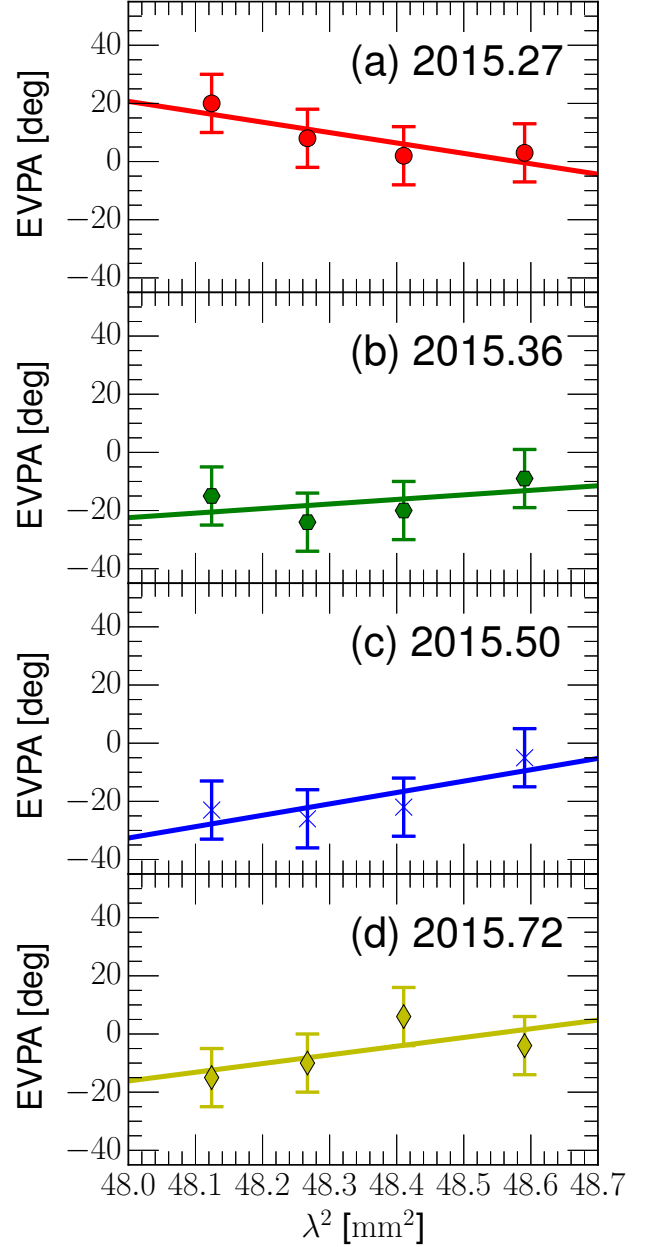


Fig. 10. EVPA of 3C 84 plotted versus the squared wavelength λ^2 within the VLBA 43 GHz band (error bars) and the best-fit Faraday rotation model (solid line).

calibration errors, the intrinsic RM of 3C 84 in this epoch would become even more negative.

4. Discussion

4.1. Polarization structure

Here we briefly discuss possible implications of the polarization structure in the core region. At 86 GHz, the two sub-nuclear polarization features, P1 and P2, have different degrees of linear polarization. In order to highlight the polarization asymmetry, we chose the 86 GHz image shown in Fig. 7 and made a transverse cut to the core region (in the E-W direction at ~ 0.1 mas downstream of the jet). From this slice, we obtained transverse total and polarization intensity profiles (Fig. 12).

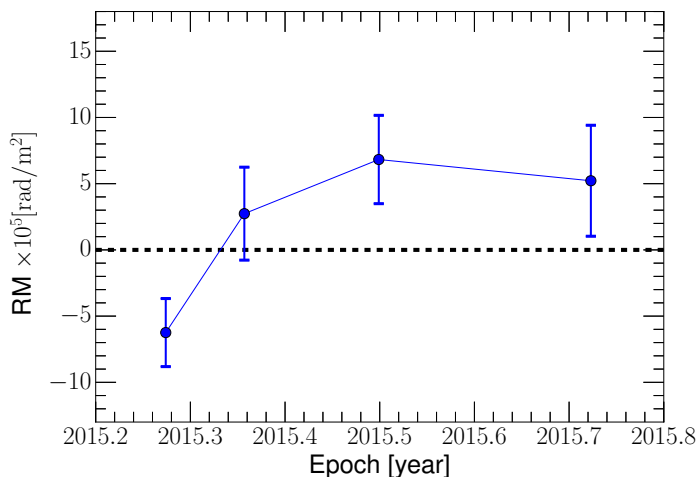


Fig. 11. Time variation of the 43 GHz sub-band RM for 3C 84.

A transverse polarization asymmetry in the core region has been occasionally seen in several other AGN (Gómez et al. 2008; O’Sullivan & Gabuzda 2009; Clausen-Brown et al. 2011; Gómez et al. 2016). This is often related to the geometry of the jet (e.g., jet inclination and opening angle) and/or the magnetic field (e.g., pitch angle; see Lyutikov et al. 2005; Clausen-Brown et al. 2011; Porth et al. 2011). We note that the intrinsic and spatially integrated EVPA is $\chi_{\text{int}} \sim -38$ deg in May 2015. This angle is neither parallel nor perpendicular to the position angle of the inner jet (~ 170 deg inferred from Fig. 7), suggesting that the orientation of the magnetic field might be oblique to the jet.

However, we also note that the polarization structure is also highly time-variable at 43 GHz during 2015 when the VLBI core flux density showed a small outburst. Such outbursts often accompany structural changes within the jet – e.g., ejection of new VLBI components from the core – and also likely lead to changes in the polarized morphology near the core. In fact, the peak of the linear polarization in the VLBA 43 GHz images moves with respect to the peak of the total intensity by ~ 0.2 mas on a \sim monthly timescale, especially in the E-W direction (see Appendix C). We note that the typical VLBA beam at 43 GHz beam is ~ 0.15 mas in E-W direction. Thus the position offset of ~ 0.2 mas is larger than the beam size and should be significant. Single-dish monitoring observations of 3C 84 at millimeter wavelengths by Agudo et al. (2018b) also show polarization time-variability on longer timescales. Therefore, one cannot rule out the possibility of turbulence (e.g., Marscher 2014) or varying opacity across the jet which may also produce similar asymmetric and variable polarization structures.

4.2. Possible explanations for the polarization spectrum and EVPA rotation

In the rest of this discussion, we focus on possible physical explanations for the observed frequency dependence of the fractional linear polarization and EVPA. Frequency dependence of the polarization properties can be explained by several scenarios. For instance, the inverted total intensity spectrum (Fig. 5, left) between 15 and 86 GHz suggests high opacity and large synchrotron self-absorption. In such jets, the emission at a higher frequency originates from a region closer to the base of the jet (e.g., Lobanov 1998). If entanglement of the magnetic field would be the main source for the low linear polarization at low

frequencies, a larger polarization degree m_L at higher frequencies could be interpreted as progressively more ordered magnetic fields in the inner jet region (e.g., Agudo et al. 2014, 2018b). Alternatively, the large synchrotron opacity in the core itself can transform the observed polarization, making the linear polarization increasing with decreasing opacity (i.e., towards shorter wavelengths; see Pacholczyk 1970; Jones & Odell 1977). In particular, the transition from optically thick to optically thin is accompanied by a ~ 90 deg flip of the EVPA (Pacholczyk 1970).

We point out, however, that the impact of Faraday rotation is also significant because Faraday depolarization is a sensitive function of the observing frequency (Burn 1966; Sokoloff et al. 1998). Certainly, Faraday rotation may be not be a unique explanation of the large EVPA rotations across the observing frequencies. However, we also find large EVPA rotation and the corresponding RM within the 43 GHz band (Fig. 10). This suggests that opacity effects alone cannot explain the results because the opacity change within the 43 GHz band is most likely small given the small fractional bandwidth of $256 \text{ MHz}/43 \text{ GHz} \sim 6 \times 10^{-3}$.

Within this perspective, the spectrum of the circular polarization in 3C 84 is also noteworthy. The inner jet of 3C 84 has a large degree of circular polarization $m_C \sim 1-3\%$ at 15–22 GHz (Homan & Wardle 2004). At higher frequencies, there are still no direct VLBI measurements of the circular polarization in this source. However, single dish observations suggest that the fractional circular polarization has a flat spectrum between centimeter and millimeter wavelengths ($m_C \sim$ a few $\times 0.1\%$ at both 5–8 GHz and 86–230 GHz; Aller et al. 2003; Myserlis et al. 2018; Agudo et al. 2010; Thum et al. 2018). As these authors suggest, the combination of low fractional linear polarization and high circular polarization is presumably produced by Faraday conversion, which is accompanied by Faraday rotation in inhomogeneous plasma that is located within (or perhaps external) to the jet (Jones & Odell 1977; Wardle & Homan 2003; MacDonald & Marscher 2018). Therefore, we investigate in the following the impact of Faraday rotation in terms of Faraday depolarization for different types of Faraday screens.

4.3. Faraday depolarization

Based on the previous discussion (Sect. 4.2), we now discuss the impact of the Faraday effect assuming different types of Faraday screens. For the central VLBI core region of 3C 84, an external Faraday screen can be located at various places. A free-free absorption disk (Walker et al. 2000), which might be clumpy (Fujita & Nagai 2017), could act as a Faraday screen. Another possibility is the accretion flow, which surrounds the central engine (Plambeck et al. 2014). We note that a radiatively inefficient accretion flow (RIAF) has been used to interpret the frequency dependence of the linear and circular polarization of Sgr A* (e.g., Bower et al. 2002; Muñoz et al. 2012), which resembles our observations of 3C 84. Finally, the host galaxy of 3C 84 (NGC 1275) contains a substantial amount of intergalactic gas, whose effect is seen on the pc-scale jet polarization at $\lesssim 22$ GHz (Taylor et al. 2006).

In the following we will model the Faraday depolarization for three very simple cases. We then will discuss their physical implication in subsequent sections 4.3.1 and 4.3.2. Let us assume three types of Faraday screens:

1. A foreground screen with a disordered magnetic field and random RM fluctuations.

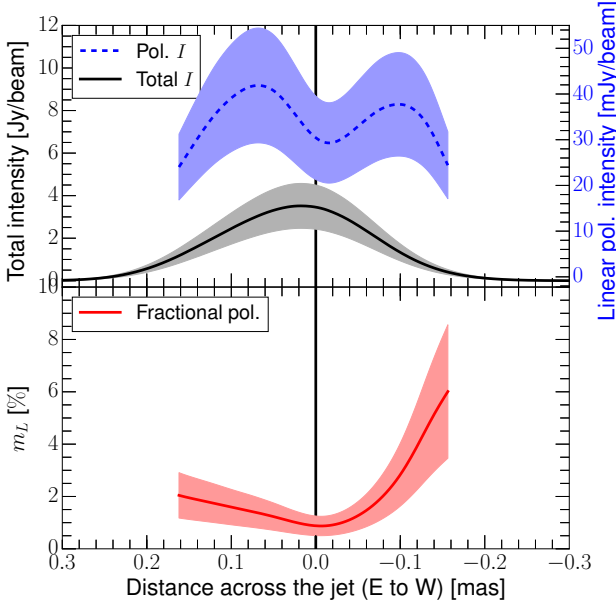


Fig. 12. (Top) total intensity, linear polarization intensity and (bottom) degree of linear polarization at 86 GHz obtained by the slice transverse to the core and calculated by the pixel values in the image plane (negative core separation towards west; see Fig. 7). The solid black line indicates position of the total intensity peak. The shaded area marks the measurement errors, assuming 30% uncertainty in the flux density measurements at 86 GHz (see Table 4). Only linear polarization higher than 24 mJy/beam is shown.

2. A foreground screen with an ordered magnetic field and a smooth RM gradient within the observing beam.
3. Faraday depolarization inside the jet and a uniform magnetic field.

Following Burn (1966), the observed degree of linear polarization m_{obs} is a function of the observing wavelength, which for the three above cases can be written as:

$$\text{Case I: } m_{obs} = m_0 \exp(-2\sigma^2\lambda^4) \quad (9)$$

$$\text{Case II: } m_{obs} = m_0 \left| \frac{\sin(\Delta RM \lambda^2)}{\Delta RM \lambda^2} \right| \quad (10)$$

$$\text{Case III: } m_{obs} = m_0 \left| \frac{\sin(2RM \lambda^2)}{2RM \lambda^2} \right| \quad (11)$$

where m_0 is the intrinsic linear polarization degree, λ is the observing wavelength, σ is the standard deviation of the dispersion of the RM in the external Faraday screen, ΔRM is the RM gradient within the beam, and RM is the observed rotation measure. For Case I, we assume $\sigma \approx \epsilon \times RM$ where ϵ is a scaling factor describing the level of the RM dispersion (i.e., larger ϵ for more inhomogeneity). We start the calculation with $\epsilon = 1$. Similarly, we assume $\Delta RM \sim RM$ for Case II. For Cases II and III, we have conservative upper limits for m_{obs} by $m_{obs} \leq m_0/(\Delta RM \lambda^2)$ and $m_{obs} \leq m_0/(2RM \lambda^2)$, respectively. We choose $m_0 = 10\%$, which is the theoretical maximum value in the case of high synchrotron opacity (Pacholczyk 1970). Finally, we take a $RM \sim 9 \times 10^5 \text{ rad/m}^2$ from Plambeck et al. (2014), which is also close to the largest RM value found in our work ($\sim 7 \times 10^5 \text{ rad/m}^2$). Then, we compare the upper limits with the observed m_L values in May 2015. For the P2 component, we use the m_L values at 86 and 43 GHz of Table 5 and adopt $m_L \lesssim 0.1\%$ as an upper limit at 15 GHz. For the P1 component, we take the

measured m_L value at 86 GHz and adopt $m_L \lesssim 0.2\%$ and $\lesssim 0.1\%$ as upper limits for 43 and 15 GHz, respectively. For both components, we use the polarization degrees as measured with the VLBA 43 GHz restoring beam.

In Fig. 13 we show the upper limits for the linear polarization degree calculated for the three depolarization models. The plots reveal several important points. In Case I (red lines), the RM dispersion σ is as large as $9 \times 10^5 \text{ rad/m}^2$ for $\epsilon \sim 1$. This is apparently problematic for both P2 and P1 because of the strong depolarization (solid red lines). We find that $\sigma \sim 2.5 \times 10^4 \text{ rad/m}^2$ is required for P2 in order to explain the observed linear polarization at 43 GHz (dashed red line). An even smaller σ would be required if the intrinsic degree of polarization m_0 is smaller than 10% for a more disordered magnetic field. A σ which is two orders of magnitude smaller than the RM (i.e., $\epsilon \lesssim (2.5 \times 10^4)/(9 \times 10^5) \sim 0.03$) indicates a highly uniform RM distribution in the external screen, which requires a well ordered large-scale magnetic field. Similar results are obtained for P1 (σ is at most $\sim 8 \times 10^4 \text{ rad/m}^2$ and $\epsilon \lesssim (8 \times 10^4)/(9 \times 10^5) \sim 0.09$). In contrast, Case II (blue lines) seems to explain the observed linear polarization in the core much better. We find that for P2 and P1 rotation measure gradients of $\Delta RM \sim 5 \times 10^5 \text{ rad/m}^2$ and $\Delta RM \sim 1.2 \times 10^6 \text{ rad/m}^2$ could explain the polarization at $\geq 43 \text{ GHz}$, respectively (dashed blue lines).

In Case III (green solid lines), the depolarization exceeds the values that we infer from our data, so we regard Case III as less likely and do not discuss it further.

Therefore, a smooth RM distribution in the external screen appears to be the most plausible scenario. We now proceed to explore the implications of the model cases I and II, trying to distinguish between them.

4.3.1. Case I : Accretion flow as the foreground screen

In the vicinity of the central black hole and depending on its covering factor, a radiatively inefficient accretion flow RIAF (e.g., Yuan & Narayan 2014) could be regarded as a good candidate for a Faraday screen. In such a flow, magneto-rotational instabilities and magnetohydrodynamic (MHD) turbulence can introduce a certain degree of inhomogeneity in the matter and magnetic field distribution (Balbus & Hawley 1991, 1998). Recently, Johnson et al. (2015) measured the linear polarization in Sgr A* with VLBI at 230 GHz and suggested a short coherence length of the magnetic field orientation, of order of $\sim 6R_s$. The linear polarization appears more random over larger scales. Adopting this also for the accretion flow of 3C 84 leads to the expectation that the Faraday depth across the screen is comparable to the characteristic Faraday depth (i.e., σ and/or $\Delta RM \sim RM$). However, this is in contrast to our finding (see Fig. 13). Certainly, our modeling simplifies a number of details in the disk-jet system. However, detailed general relativistic MHD simulations of such an accretion flow also suggest very strong depolarization of the jet by the accretion flow (e.g., Mościbrodzka et al. 2017). Hence, the accretion flow appears to us as a less preferred candidate for the Faraday screen.

Another problem in the association of the large RM in 3C 84 with the accretion flow was pointed out by Plambeck et al. (2014). The authors modeled a spherical accretion flow in 3C 84 using a highly ordered, radial magnetic field, in order to relate the observed $RM \sim 9 \times 10^5 \text{ rad/m}^2$ with the expected mass accretion rate. For realistic estimates of the magnetic field strength and the electron density in the accretion flow, the authors derive a higher RM, so that the observed RM appears to be too small. Therefore, the authors concluded that either (i) the mag-

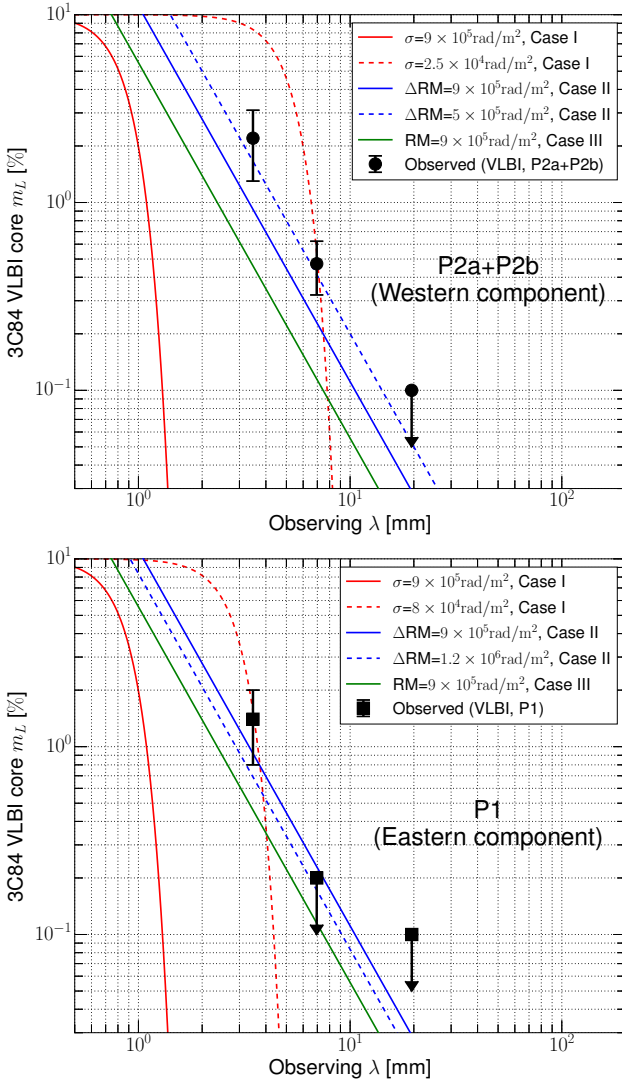


Fig. 13. Upper limits for m_L for external (Case I and II) and internal (Case III) Faraday depolarization and the VLBI polarization from observations. Arrows indicate upper limit from observations. The top and bottom panels are for the P2 and P1 components, respectively. See the text for the details.

netic field strength is much weaker than the equipartition value, (ii) the magnetic field is highly disordered, and/or (iii) the accretion flow is rather disk-like and the line of sight does not pass through the accretion flow. Indeed, an oblate disk-like geometry of the accretion flow would provide a suitable explanation because it explains the observational findings without fine-tuning the intrinsic physical properties of the accretion flow.

If the observed linear polarization is marginally affected by the disk-like accretion flow because of the geometry, the disk height H to disk radius R ratio H/R should be $\tan^{-1}(H/R) \lesssim (90^\circ - \theta)$ or $H/R \lesssim \tan(90^\circ - \theta)$ where θ is the jet viewing angle. If we adopt $\theta \sim 30^\circ$ ($\sim 60^\circ$) from previous observations (Walker et al. 1994; Fujita & Nagai 2017), we find $H/R \lesssim 1.7$ ($\lesssim 0.6$). If the thick accretion flow is threaded by a strong poloidal magnetic field which can compress the disk vertically (e.g., McKinney et al. 2012), an even smaller H/R ratio may be physically possible.

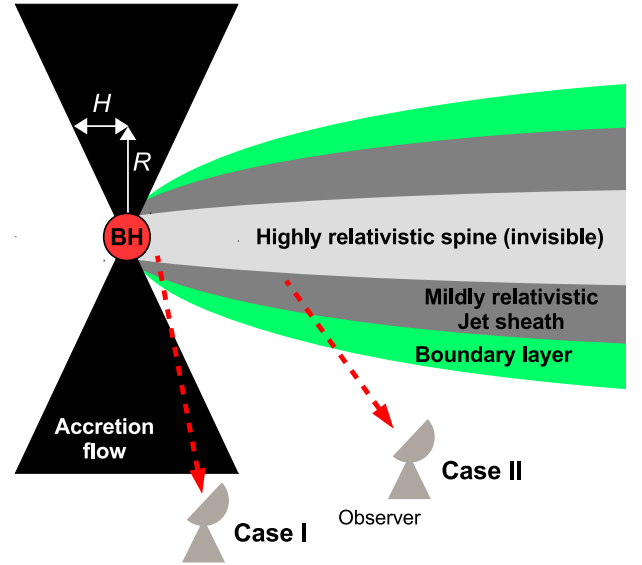


Fig. 14. Illustration of the geometry discussed throughout Sect. 4.3.1 and 4.3.2. Note that the figure is not drawn to scale.

4.3.2. Case II : Faraday rotation & depolarization due to the transverse jet stratification

Alternatively, a mildly-relativistic sheath surrounding the relativistic jet may provide the required external screen. A wide and collimated jet can be formed by the inner accretion disk or directly by spinning central black hole (Blandford & Payne 1982; Blandford & Znajek 1977). The rotation of the central engine leads to the development of a stratified and twisted magnetic field topology (e.g., Tchekhovskoy 2015). The boundary layer (or sheath) of such jets may provide the uniform external Faraday screen in Case II. Evidence for an ordered magnetic field configuration in jets comes from a plethora of polarization VLBI jet observations and from observations of transverse RM gradients on pc scales (e.g., Zavala & Taylor 2005; Hovatta et al. 2012; Gabuzda et al. 2017). The magnetic field is expected to be more ordered in the inner jet region when the jet launching region becomes magnetically dominated (e.g., Zamaninasab et al. 2014; Martí-Vidal et al. 2015).

High angular resolution VLBI observations of the inner jet of 3C 84 show a limb-brightened morphology (see Fig. 7 and also Giovannini et al. 2018). A limb-brightened jet most likely consists of at least two different jet components with different speeds, electron densities and/or magnetic field strengths (spine-sheath geometry; e.g., Pelletier & Roland 1989; Komissarov 1990). Mildly relativistic electrons in the boundary layer of the jet, possibly mixed with thermal particles, will then cause Faraday rotation and conversion (Sokoloff et al. 1998; Perlman et al. 1999; Pushkarev et al. 2005; Porth et al. 2011; MacDonald et al. 2015; Pasetto et al. 2016; Lico et al. 2017). In Figure 14 we show a sketch of a stratified jet for illustration.

4.4. Estimation of the jet magnetic field strength and the electron density

In the following we assume that the boundary layer of the jet is the Faraday screen and is responsible for the observed RM. We estimate the jet electron number density adopting the jet magnetic field strength from the synchrotron self-absorption theory.

In convenient units, the observed RM can be written as follows:

$$\frac{\text{RM}}{\text{rad/m}^2} = 8.1 \times 10^5 \int_{\text{source}}^{\text{telescope}} \left(\frac{n_e}{\text{cm}^{-3}} \right) \left(\frac{B_{\parallel}}{\text{G}} \right) \left(\frac{dl}{\text{pc}} \right) \quad (12)$$

where n_e is the number density of the thermal electrons between the source and the telescope, B_{\parallel} is the line-of-sight component of the magnetic field, and dl is the path length through the plasma from the source toward the observer.

We calculate the synchrotron self-absorption (SSA) magnetic field strength B_{SSA} in the core following Marscher (1983);

$$B_{SSA} = 10^{-5} b(\alpha) \frac{\theta_m^4 \nu_m^5 \delta}{S_m^2 (1+z)} \quad \text{Gauss} \quad (13)$$

where $b(\alpha)$ is a constant tabulated in Marscher (1983) as a function of the spectral index, S_m is the flux density (in Jy) at the turn-over frequency ν_m (in GHz), θ_m is the source angular size (in mas) at ν_m , and δ is the Doppler factor. We note that the exact value of ν_m is not accurately determined by our data (see the spectrum in Fig. 5). However, this spectrum and recent VLBI observations of 3C 84 at 86 GHz and 129 GHz (Hodgson et al. 2018) suggest a spectral turnover near 86 GHz. Therefore, we adopt $\nu_m = 86$ GHz for the calculation of B_{SSA} . For the optically thin spectrum we use $\alpha = -0.5$, which fixes $b(\alpha) = 3.2$. Assuming $\nu_m = 86$ GHz, $S_m = (5.6 \pm 1.7)$ Jy, and $\theta_m = 1.8 \times (0.14 \pm 0.01) \text{ mas}^7$, we obtain $B_{SSA} \sim (19 \pm 13) \times \delta$ G.

For the jet viewing angle $\theta \sim 30^\circ - 60^\circ$ and the apparent jet speed $\sim 0.1c$ near the core, the Doppler factor is $\delta \sim 1.1$. With this, we obtain $B_{SSA} \sim (21 \pm 14)$ G. We note that Abdo et al. (2009) and Aleksić et al. (2014) suggest a rather large Doppler factor of $\delta \sim 2 - 4$ based on the theoretical modeling of the synchrotron self-Compton process in the jet. In this case, the resulting magnetic field strength would be $\sim (2 - 4)$ times larger.

We take B_{SSA} as the average magnetic field strength in the jet and calculate the average electron number density n_e by

$$\frac{n_e}{\text{cm}^{-3}} \sim 1.2 \times 10^{-6} \left(\frac{\text{RM}}{\text{rad/m}^2} \right) \left(\frac{B_{SSA}}{\text{G}} \right)^{-1} \left(\frac{\theta_m}{\text{pc}} \right)^{-1} \quad (14)$$

where we assume that the size θ_m is a lower limit to the approximate pathlength for the jet medium because a longer pathlength is expected for a deprojected line-of-sight. For $\text{RM} = 9 \times 10^5 \text{ rad/m}^2$, we obtain $n_e \leq (0.6 \pm 0.4) \text{ cm}^{-3}$. The density will be even lower if the Doppler factor is larger and the magnetic field strength is higher. In any case, the density is an order of magnitude lower than an ambient gas density estimate of $n_e \sim 8 \text{ cm}^{-3}$ obtained by Fujita & Nagai (2017) for the central parsecs. A low jet density is not implausible and is consistent with jet collimation by a denser ambient medium (e.g., Nagai et al. 2014; Giovannini et al. 2018).

We note that our calculations make simplified assumptions with regards to the magnetic field strength, the path length, and the jet geometry. Future more detailed calculations using numerical radiative transfer across all Stokes parameters (e.g., MacDonald & Marscher 2018) should be able to constrain these parameters more precisely. Also, the exact value of the turn-over frequency on this spatial scale is still quite uncertain. Quasi-simultaneous global mm-VLBI observations with the GMVA and the Event Horizon Telescope (e.g., Doeleman et al. 2012; Lu et al. 2018) will help to determine the spectral properties of the innermost jet and central engine.

⁷ The factor 1.8 corrects for the geometry (Marscher 1983).

5. Summary and Conclusions

In this paper, we presented a study of the polarization properties of the radio galaxy 3C 84 based on the results from polarimetric VLBI observations of the source at mm-wavelengths. We summarize our findings and main conclusions as follows:

1. We found asymmetrically distributed and polarized emission in the VLBI core region of 3C 84 at 86 GHz using GMVA observations. The east-west oriented and linearly polarized structure consists of two polarized components (P1 and P2), which are separated by ~ 0.2 mas (corresponding to $\sim 0.07 \text{ pc} \sim 812 R_s$). The fractional linear polarization m_L of P1 and P2 at 86 GHz is $\sim 2\%$ with the VLBA 43 GHz beam.
2. Additional close-in-time VLBA 43 GHz polarization images also reveal the presence of polarized emission ($m_L \sim 0.4 - 0.5\%$). The polarized structure is also time-variable. The moving direction of the variable polarized emission feature, which is almost perpendicular to the milli-arcsecond jet, suggests that the jet base may be edge-brightened in polarized light. However, other effects such as ejection of a new VLBI component or opacity effects across the jet cannot be excluded.
3. The total intensity spectrum of 3C 84 is inverted up to at least 86 GHz and the linear polarization m_L increases with frequency following a power-law $m_L \propto \nu^{0.77}$. A likely explanation invokes a decreasing synchrotron opacity and lower Faraday depolarization at higher frequencies.
4. The combination of quasi-simultaneous EVPA measurements at 43 GHz and 86 GHz, and adding near in time EVPA measurements from ALMA at higher frequencies, reveals a high rotation measure in the VLBI core region of $\text{RM} \sim 2 \times 10^5 \text{ rad/m}^2$ at ≥ 43 GHz in May 2015. This is comparable to the RM measurements at 230 GHz on larger angular scales (Plambeck et al. 2014).
5. A significant rotation of the EVPA is also observed within the 43 GHz VLBA observing band and also suggests the presence of Faraday rotation. Repeated measurements of the RM within the 43 GHz VLBA observing band are consistent with the high RM in the VLBI core region at three epochs, but also suggest that the RM has changed its sign at one epoch. This could be related to the onset of a small total intensity flare in the VLBI core in 2015.
6. In order to explain the degree of linear polarization by Faraday depolarization, an external screen with either a small RM dispersion or only a smoothly varying uniform RM distribution is required.
7. The data would support a tentative association of the Faraday screen with the accretion flow if (i) the accretion flow is thick ($H/R \geq 1.7$ for the jet viewing angle $\theta = 30^\circ$) and more importantly (ii) the magnetic field is highly ordered. However, the latter appears to be in contradiction with the results of previous studies (e.g., Plambeck et al. 2014). Instead, a stratified jet with a boundary layer containing an ordered magnetic field configuration could also provide a good explanation for the large RM, the frequency dependence of the depolarization, and possibly also for the RM variability. The edge-brightened jet morphology observed at 22 GHz (Giovannini et al. 2018) would also support this interpretation.
8. From synchrotron self-absorption theory, we calculate a magnetic field strength in the VLBI core region of 3C 84 of $B_{SSA} = (21 \pm 14)$ G, adopting an only mild relativistic beaming with a Doppler factor of $\delta \sim 1.1$ from jet kinematics. In this case a jet electron density of $n_e \leq (0.6 \pm 0.4) \text{ cm}^{-3}$ is

required to explain the observed high RM. The field strength would be larger by factor $\sim 2-4$ if a higher Doppler factor of $\delta \sim 2-4$ is used, and the electron density will be correspondingly lower. In both cases the jet electron density appears to be at least an order of magnitude lower than the density of the ambient gas.

Overall, our study suggests that either the accretion flow or a transversely stratified jet with boundary layers can play an important role in the generation of the polarized mm-wave emission in the milli-parsec scale VLBI structure. Future millimeter VLBI imaging, performed quasi-simultaneously at different frequencies and including VLBI observations above 86 GHz, will help to better understand the complicated nature of the polarization in 3C 84. Also, a more detailed theoretical modeling of the linear and circular polarization spectrum, and complemented by numerical simulations, would be very beneficial. Finally, we note that the detection of significant linear polarization at the jet base in 3C 84 may shed light on the properties of the Faraday screen in other radio galaxies (e.g., M87; Kim et al. 2018). Further studies should prove fruitful.

Acknowledgements. We thank the anonymous referee for valuable comments and suggestions, which greatly helped to improve the paper. We thank Carolina Casadio and Ioannis Myserlis for fruitful discussions and comments. J.-Y.K. is supported for this research by the International Max-Planck Research School (IMPRS) for Astronomy and Astrophysics at the University of Bonn and Cologne. I.A. acknowledges support by a Ramón y Cajal grant of the Ministerio de Economía, Industria y Competitividad (MINECO) of Spain, and by additional MINECO grant with reference AYA2016-80889-P. R.-S. L. is supported by the National Youth Thousand Talents Program of China and by the Max-Planck Partner Group. This research has made use of data obtained with the Global Millimeter VLBI Array (GMVA), which consists of telescopes operated by the MPIfR, IRAM, Onsala, Metsahovi, Yebes, the Korean VLBI Network, the Green Bank Observatory and the Long Baseline Observatory. The VLBA is an instrument of the Long Baseline Observatory, which is a facility of the National Science Foundation operated by Associated Universities, Inc. The data were correlated at the correlator of the MPIfR in Bonn, Germany. This work made use of the Swinburne University of Technology software correlator, developed as part of the Australian Major National Research Facilities Programme and operated under licence. This study makes use of 43 GHz VLBA data from the VLBA-BU Blazar Monitoring Program (VLBA-BU-BLAZAR; <http://www.bu.edu/blazars/VLBAproject.html>), funded by NASA through the Fermi Guest Investigator Program. This research has made use of data from the MOJAVE database that is maintained by the MOJAVE team (Lister et al. 2009). This paper makes use of the following ALMA data: ADS/JAO.ALMA#2011.0.00001.CAL. ALMA is a partnership of ESO (representing its member states), NSF (USA) and NINS (Japan), together with NRC (Canada), MOST and ASIAA (Taiwan), and KASI (Republic of Korea), in cooperation with the Republic of Chile. The Joint ALMA Observatory is operated by ESO, AUI/NRAO and NAOJ. This research has made use of data from the OVRO 40 m monitoring program (Richards et al. 2011). The OVRO 40 M Telescope Fermi Blazar Monitoring Program is supported by NASA under awards NNX08AW31G and NNX11A043G, and by the NSF under awards AST-0808050 and AST-1109911.

References

Abdo, A. A., Ackermann, M., Ajello, M., et al. 2009, *ApJ*, 699, 31
 Agudo, I., Marscher, A. P., Jorstad, S. G., et al. 2012, *ApJ*, 747, 63
 Agudo, I., Thum, C., Gómez, J. L., & Wiesenmeyer, H. 2014, *A&A*, 566, A59
 Agudo, I., Thum, C., Molina, S. N., et al. 2018a, *MNRAS*, 474, 1427
 Agudo, I., Thum, C., Ramakrishnan, V., et al. 2018b, *MNRAS*, 473, 1850
 Agudo, I., Thum, C., Wiesenmeyer, H., & Krichbaum, T. P. 2010, *ApJS*, 189, 1
 Aleksić, J., Ansoldi, S., Antonelli, L. A., et al. 2014, *A&A*, 564, A5
 Aller, H. D., Aller, M. F., & Plotkin, R. M. 2003, *Ap&SS*, 288, 17
 Balbus, S. A. & Hawley, J. F. 1991, *ApJ*, 376, 214
 Balbus, S. A. & Hawley, J. F. 1998, *Reviews of Modern Physics*, 70, 1
 Blandford, R. D. & Payne, D. G. 1982, *MNRAS*, 199, 883
 Blandford, R. D. & Znajek, R. L. 1977, *MNRAS*, 179, 433
 Boccardi, B., Krichbaum, T. P., Ros, E., & Zensus, J. A. 2017, *Astronomy and Astrophysics Review*, 25, 4
 Bower, G. C., Falcke, H., Sault, R. J., & Backer, D. C. 2002, *ApJ*, 571, 843

Burn, B. J. 1966, *MNRAS*, 133, 67
 Casadio, C., Gómez, J. L., Jorstad, S. G., et al. 2015, *ApJ*, 813, 51
 Casadio, C., Krichbaum, T., Marscher, A., et al. 2017, *Galaxies*, 5, 67
 Clausen-Brown, E., Lyutikov, M., & Kharb, P. 2011, *MNRAS*, 415, 2081
 Deller, A. T., Brisken, W. F., Phillips, C. J., et al. 2011, *Publications of the Astronomical Society of the Pacific*, 123, 275
 Doeleman, S. S., Fish, V. L., Schenck, D. E., et al. 2012, *Science*, 338, 355
 Fujita, Y. & Nagai, H. 2017, *MNRAS*, 465, L94
 Gabuzda, D. C., Roche, N., Kirwan, A., et al. 2017, *MNRAS*, 472, 1792
 Giovannini, G., Savolainen, T., Orienti, M., et al. 2018, *Nature Astronomy*, 33
 Gómez, J. L., Lobanov, A. P., Bruni, G., et al. 2016, *ApJ*, 817, 96
 Gómez, J. L., Marscher, A. P., Jorstad, S. G., Agudo, I., & Roca-Sogorb, M. 2008, *ApJ*, 681, L69
 Greisen, E. W. 1990, in *Acquisition, Processing and Archiving of Astronomical Images*, ed. G. Longo & G. Sedmak, 125–142
 Hodgson, J. A., Krichbaum, T. P., Marscher, A. P., et al. 2017, *A&A*, 597, A80
 Hodgson, J. A., Rani, B., Lee, S.-S., et al. 2018, *MNRAS*, 475, 368
 Homan, D. C. & Wardle, J. F. C. 2004, *ApJ*, 602, L13
 Hovatta, T., Lister, M. L., Aller, M. F., et al. 2012, *AJ*, 144, 105
 Jackson, N., Browne, I. W. A., Battye, R. A., Gabuzda, D., & Taylor, A. C. 2010, *MNRAS*, 401, 1388
 Johnson, M. D., Fish, V. L., Doeleman, S. S., et al. 2015, *Science*, 350, 1242
 Jones, T. W. & Odell, S. L. 1977, *ApJ*, 214, 522
 Jorstad, S. G., Marscher, A. P., Lister, M. L., et al. 2005, *AJ*, 130, 1418
 Jorstad, S. G., Marscher, A. P., Morozova, D. A., et al. 2017, *ApJ*, 846, 98
 Jorstad, S. G., Marscher, A. P., Stevens, J. A., et al. 2007, *AJ*, 134, 799
 Kim, J. Y., Krichbaum, T. P., Lu, R. S., et al. 2018, *A&A*, 616, A188
 Komissarov, S. S. 1990, *Soviet Astronomy Letters*, 16, 284
 Koyama, S., Kino, M., Giroletti, M., et al. 2016, *A&A*, 586, A113
 Leppanen, K. J., Zensus, J. A., & Diamond, P. J. 1995, *AJ*, 110, 2479
 Lico, R., Gómez, J. L., Asada, K., & Fuentes, A. 2017, *MNRAS*, 469, 1612
 Lister, M. L., Aller, H. D., Aller, M. F., et al. 2009, *AJ*, 137, 3718
 Lister, M. L. & Homan, D. C. 2005, *AJ*, 130, 1389
 Lobanov, A. P. 1998, *A&A*, 330, 79
 Lu, R.-S., Krichbaum, T. P., Roy, A. L., et al. 2018, *ApJ*, 859, 60
 Lyutikov, M., Pariev, V. I., & Gabuzda, D. C. 2005, *MNRAS*, 360, 869
 MacDonald, N. R. & Marscher, A. P. 2018, *ApJ*, 862, 58
 MacDonald, N. R., Marscher, A. P., Jorstad, S. G., & Joshi, M. 2015, *ApJ*, 804, 111
 Marscher, A. P. 1983, *ApJ*, 264, 296
 Marscher, A. P. 2014, *ApJ*, 780, 87
 Martí-Vidal, I., Krichbaum, T. P., Marscher, A., et al. 2012, *A&A*, 542, A107
 Martí-Vidal, I., Muller, S., Vlemmings, W., Horellou, C., & Aalto, S. 2015, *Science*, 348, 311
 McKinney, J. C., Tchekhovskoy, A., & Blandford, R. D. 2012, *MNRAS*, 423, 3083
 Montier, L., Plaszczyński, S., Levrier, F., et al. 2015a, *A&A*, 574, A135
 Montier, L., Plaszczyński, S., Levrier, F., et al. 2015b, *A&A*, 574, A136
 Mościbrodzka, M., Dexter, J., Davelaar, J., & Falcke, H. 2017, *MNRAS*, 468, 2214
 Muñoz, D. J., Marrone, D. P., Moran, J. M., & Rao, R. 2012, *ApJ*, 745, 115
 Myserlis, I., Angelakis, E., Kraus, A., et al. 2018, *A&A*, 609, A68
 Nagai, H., Fujita, Y., Nakamura, M., et al. 2017, *ApJ*, 849, 52
 Nagai, H., Haga, T., Giovannini, G., et al. 2014, *ApJ*, 785, 53
 O’Sullivan, S. P. & Gabuzda, D. C. 2009, *MNRAS*, 393, 429
 Pacholczyk, A. G. 1970, *Radio astrophysics. Nonthermal processes in galactic and extragalactic sources*
 Pasetto, A., Carrasco-González, C., Bruni, G., et al. 2016, *Galaxies*, 4, 66
 Pelletier, G. & Roland, J. 1989, *A&A*, 224, 24
 Perlman, E. S., Biretta, J. A., Zhou, F., Sparks, W. B., & Macchetto, F. D. 1999, *AJ*, 117, 2185
 Plambeck, R. L., Bower, G. C., Rao, R., et al. 2014, *ApJ*, 797, 66
 Porth, O., Fendt, C., Meliani, Z., & Vaidya, B. 2011, *ApJ*, 737, 42
 Pushkarev, A. B., Gabuzda, D. C., Vetukhnovskaya, Y. N., & Yakimov, V. E. 2005, *MNRAS*, 356, 859
 Rani, B., Krichbaum, T. P., Marscher, A. P., et al. 2015, *A&A*, 578
 Richards, J. L., Max-Moerbeck, W., Pavlidou, V., et al. 2011, *The Astrophysical Journal Supplement Series*, 194
 Roberts, D. H., Wardle, J. F. C., & Brown, L. F. 1994, *ApJ*, 427, 718
 Scharwächter, J., McGregor, P. J., Dopita, M. A., & Beck, T. L. 2013, *MNRAS*, 429, 2315
 Schinzel, F. K., Lobanov, A. P., Taylor, G. B., et al. 2012, *A&A*, 537, A70
 Shepherd, M. C., Pearson, T. J., & Taylor, G. B. 1994, in *BAAS*, Vol. 26, *Bulletin of the American Astronomical Society*, 987–989
 Sokoloff, D. D., Bykov, A. A., Shukurov, A., et al. 1998, *MNRAS*, 299, 189
 Strauss, M. A., Huchra, J. P., Davis, M., et al. 1992, *ApJS*, 83, 29
 Suzuki, K., Nagai, H., Kino, M., et al. 2012, *ApJ*, 746, 140
 Taylor, G. B., Gugliucci, N. E., Fabian, A. C., et al. 2006, *MNRAS*, 368, 1500

- Tchekhovskoy, A. 2015, in *Astrophysics and Space Science Library*, Vol. 414, The Formation and Disruption of Black Hole Jets, ed. I. Contopoulos, D. Gabuzda, & N. Kylafis, 45
- Thompson, A. R., Moran, J. M., & Swenson, George W., J. 2017, *Interferometry and Synthesis in Radio Astronomy*, 3rd Edition
- Thum, C., Agudo, I., Molina, S. N., et al. 2018, *MNRAS*, 473, 2506
- Thum, C., Wiesemeyer, H., Paubert, G., Navarro, S., & Morris, D. 2008, *PASP*, 120, 777
- Trippe, S., Bremer, M., Krichbaum, T. P., et al. 2012, *MNRAS*, 425, 1192
- Walker, R. C., Dhawan, V., Romney, J. D., Kellermann, K. I., & Vermeulen, R. C. 2000, *ApJ*, 530, 233
- Walker, R. C., Romney, J. D., & Benson, J. M. 1994, *ApJ*, 430, L45
- Wardle, J. F. C. & Homan, D. C. 2003, *Ap&SS*, 288, 143
- Wardle, J. F. C. & Kronberg, P. P. 1974, *ApJ*, 194, 249
- Yuan, F. & Narayan, R. 2014, *ARA&A*, 52, 529
- Zamaninasab, M., Clausen-Brown, E., Savolainen, T., & Tchekhovskoy, A. 2014, *Nature*, 510, 126
- Zavala, R. T. & Taylor, G. B. 2005, *ApJ*, 626, L73

Appendix A: On the flux density calibration of 3C 84 using 86 GHz GMVA data in May 2015

Here we discuss a method to improve the accuracy of the absolute flux density calibration of 3C 84 at 86 GHz based on the available a-priori GMVA amplitude calibration, which is not accurate enough (see also Koyama et al. 2016). We compared the multi-frequency VLBI flux densities of 3C 84 (Sect. 2.1 and 2.2) with the total flux densities measured by other instruments. At $\nu = 15$ GHz, the Owens Valley Radio Observatory (OVRO; Richards et al. 2011) monitoring program⁸ provided near-in-time flux density measurements of $S = 31.8 \pm 0.5$ Jy and $S = 32.3 \pm 0.1$ Jy for 3C 84 on 03 Apr 2015 and 27 Jun 2015, respectively. We averaged the two fluxes in order to estimate the total flux in May 2015 and took half of their difference as the associated error, finding $S = 32.1 \pm 0.3$ Jy. At $\nu \gtrsim 86$ GHz, we refer to Sect. 2.4 for the ALMA flux density measurements. In Fig. A.1 we show (i) the VLBI-scale flux density of the source within ~ 4 mas from the core (S_{VLBI}), (ii) the VLBI-scale flux density only for the extended jet ($\sim 2 - 4$ mas from the core; S_{Jet}), and (iii) the total (i.e., spatially unresolved) flux density measured by the OVRO and the ALMA observations (S_{tot}). The GMVA flux densities were taken from only the self-calibrated data, based on the a-priori calibration. We fitted a power-law model to the total flux density (i.e., $S_{\text{VLBI}} \propto \nu^{\alpha}$) in order to estimate the VLBI flux density S_{VLBI} at 43 and 86 GHz. The total flux density spectrum is fitted by $S_{\text{tot}} \propto \nu^{-(0.45 \pm 0.04)}$. From this we estimate S_{tot} at 43 GHz and 86 GHz and calculated the VLBI-to-total flux density ratio $S_{\text{VLBI}}/S_{\text{tot}}$ (i.e., the compactness). At 15 GHz and 43 GHz, the flux ratio is comparable (~ 0.90 and ~ 0.84 at 15 GHz and 43 GHz, respectively). However at 86 GHz, it is much lower ($S_{\text{VLBI}}/S_{\text{tot}} \sim 0.40$). The comparison of the spectral index of the extended jet emission yields a spectral index of $\alpha_{15-43 \text{ GHz}} \sim -0.5$, while the spectral index from 43 GHz to 86 GHz is much steeper; $\alpha_{43-86 \text{ GHz}} \sim -1.8$. Such a steep spectrum is unlikely, and is inconsistent with ALMA measurements between 98 GHz and 344 GHz. We therefore take this as another indication for a too low flux densities at 86 GHz,

To check for an overall scaling problem of the GMVA amplitude calibration we examined the compactness ratio $S_{\text{VLBI}}/S_{\text{tot}}$ also for other calibrators at 86 GHz (3C 454.3, BLLac, CTA 102, and OJ 287), for which we find – applying a similar procedure as described above – compactness ratios of typically 0.9 at 15 GHz and 43 GHz, but ~ 0.5 at 86 GHz. In the following we assume that the true compactness $S_{\text{VLBI}}/S_{\text{tot}}$ at 15, 43, and 86 GHz is comparable. Then the visibility amplitudes of the GMVA data of 3C 84 can be upscaled by a factor $g \sim 2.1 - 2.3$. Confidence for this number also come from similar factors obtained for the other calibrators. With this correction factor a much more realistic value of the (optically thin) jet spectral index $\alpha_{43-86 \text{ GHz}} \sim -0.8$ is obtained. The corrected total flux density (~ 12 Jy) is now also in good agreement with other near-in-time VLBI flux density measurements at 86 GHz reported in literature (e.g., $S \sim (10 - 15)$ Jy; see Hodgson et al. 2018).

In the following we discuss the uncertainty Δg of the scaling value g , which depends on the validity of our assumptions, and we could alternatively assume the same spectral index from 15 GHz to 86 GHz for S_{Jet} . Assuming a constant spectral index $\alpha_{15-86 \text{ GHz}} \sim -0.5$ results in a slightly larger correction factor of $g \sim 2.5$. The range of the $g \sim 2.1 - 2.5$ suggests that its uncertainty is $\Delta g \sim 0.4$, corresponding to a $\sim 20\%$ of error in the absolute flux density. It would be overly optimistic to claim an

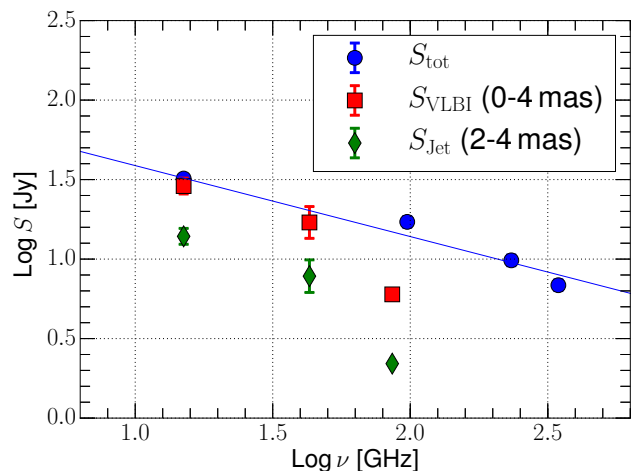


Fig. A.1. Quasi-simultaneous total and VLBI-scale flux densities of 3C 84 in May 2015 displayed in log-log scale. The blue solid line shows the power-law fitted to the total flux measurements. We omit the error bars for the GMVA 86 GHz data points.

error smaller than $\sim 20\%$ without having identified the origin of the amplitude scaling error. Therefore, we adopted a slightly larger value of $\sim 30\%$ for the systematic uncertainty in the measured VLBI flux densities (for this particular epoch).

Appendix B: Robustness of the polarization imaging at 86 GHz

In order to illustrate the impact of slightly different D-terms on the polarization image of the GMVA data, we made different linear polarization images of 3C 84 using D-terms determined from the individual calibrators. Two examples are shown in Fig. B.1. We find that two central polarization features are reproduced in the nuclear region at similar locations with similar EVPAs. We note that the structure of the jet of OJ 287 is substantially different from that of CTA 102 (e.g., Agudo et al. 2012; Casadio et al. 2015; Hodgson et al. 2017). Despite this, the two polarization maps shown in Fig. B.1 look similar, which provides confidence of the polarization calibration and imaging of 3C 84. Nevertheless, we consider that the polarization image in the main text, which is obtained with the averaged D-terms, is of better quality than those in Fig. B.1 for the reasons explained in the main text.

Appendix C: Multi-epoch VLBA 43 GHz data

In Table C.1 we show the results of the VLBA 43 GHz polarization measurements in the four different epochs. We provide the polarization maps of the corresponding epochs obtained from the frequency-averaged visibilities in Fig. C.1. The core flux and the FWHM size during 2015 are given in Table C.2.

⁸ <http://www.astro.caltech.edu/ovroblazars/>

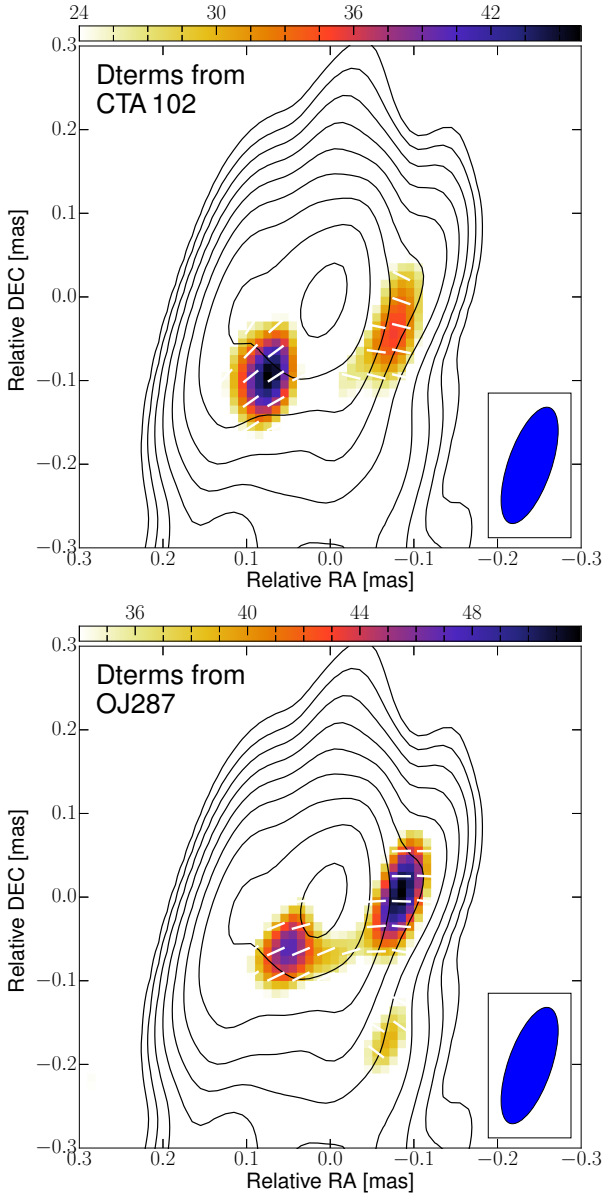


Fig. B.1. Linear polarization maps of the nuclear region of 3C 84 at 86 GHz obtained with different polarization calibrations. The two maps were reconstructed using the D-terms obtained from CTA 102 (upper panel) and from OJ 287 (lower panel), respectively. The minimum contour level is 7 mJy/beam.

Table C.1. Properties of the polarized components at 43 GHz obtained from the polarization imaging at four different IFs. The columns show (1) the observing epoch, (2) the observing frequency at each IF, (3) the total flux, (4) the degree of linear polarization, and (5) the EVPA. The total flux was consistent across the frequency in each epoch and we report the measurement only for a single IF.

Epoch (1) [yyyy/mm/dd]	ν_{obs} (2) [GHz]	S_v^a (3) [Jy]	m_L (4) [%]	χ (5) [deg]
2015/04/11	43.0075	1.4 ± 0.1	0.73 ± 0.23	3 ± 10
	43.0875		0.76 ± 0.24	2 ± 10
	43.1515		0.61 ± 0.19	8 ± 10
	43.2155		0.32 ± 0.10	20 ± 10
2015/05/11	43.0075	2.0 ± 0.2	0.44 ± 0.14	$-(9 \pm 10)$
	43.0875		0.49 ± 0.16	$-(20 \pm 10)$
	43.1515		0.53 ± 0.17	$-(24 \pm 10)$
	43.2155		0.43 ± 0.13	$-(15 \pm 10)$
2015/07/02	43.0075	3.6 ± 0.4	0.37 ± 0.12	$-(5 \pm 10)$
	43.0875		0.40 ± 0.13	$-(22 \pm 10)$
	43.1515		0.67 ± 0.21	$-(26 \pm 10)$
	43.2155		0.47 ± 0.15	$-(23 \pm 10)$
2015/09/22	43.0075	2.8 ± 0.3	0.28 ± 0.09	$-(4 \pm 10)$
	43.0875		0.37 ± 0.10	6 ± 10
	43.1515		0.33 ± 0.11	$-(10 \pm 10)$
	43.2155		0.38 ± 0.12	$-(15 \pm 10)$

Notes. ^(a) The time-variable total flux density of the polarized component is due to not only the flux variability but also the different positions of the peak of the polarization.

Table C.2. The unpolarized core flux (in Jy), the peak (in Jy/beam), and the core FWHM size (in mas) during 2015 measured from the archival VLBA 43 GHz data sets by the model-fitting analysis. A circular beam of 0.3 mas was used for all epochs.

Epoch [yyyy/mm/dd]	Flux [Jy]	Peak [Jy/beam]	FWHM size [mas]
2015/02/14	3.9 ± 0.7	3.6 ± 0.5	0.12 ± 0.01
2015/04/11	4.5 ± 0.6	4.1 ± 0.4	0.13 ± 0.01
2015/05/11	4.8 ± 0.7	4.4 ± 0.4	0.13 ± 0.01
2015/06/09	5.8 ± 0.6	5.2 ± 0.4	0.14 ± 0.01
2015/07/02	5.8 ± 0.6	5.2 ± 0.4	0.16 ± 0.01
2015/08/01	5.0 ± 0.5	4.5 ± 0.3	0.16 ± 0.01
2015/09/22	5.0 ± 0.6	4.4 ± 0.4	0.16 ± 0.01
2015/12/05	4.1 ± 0.5	3.7 ± 0.3	0.15 ± 0.01

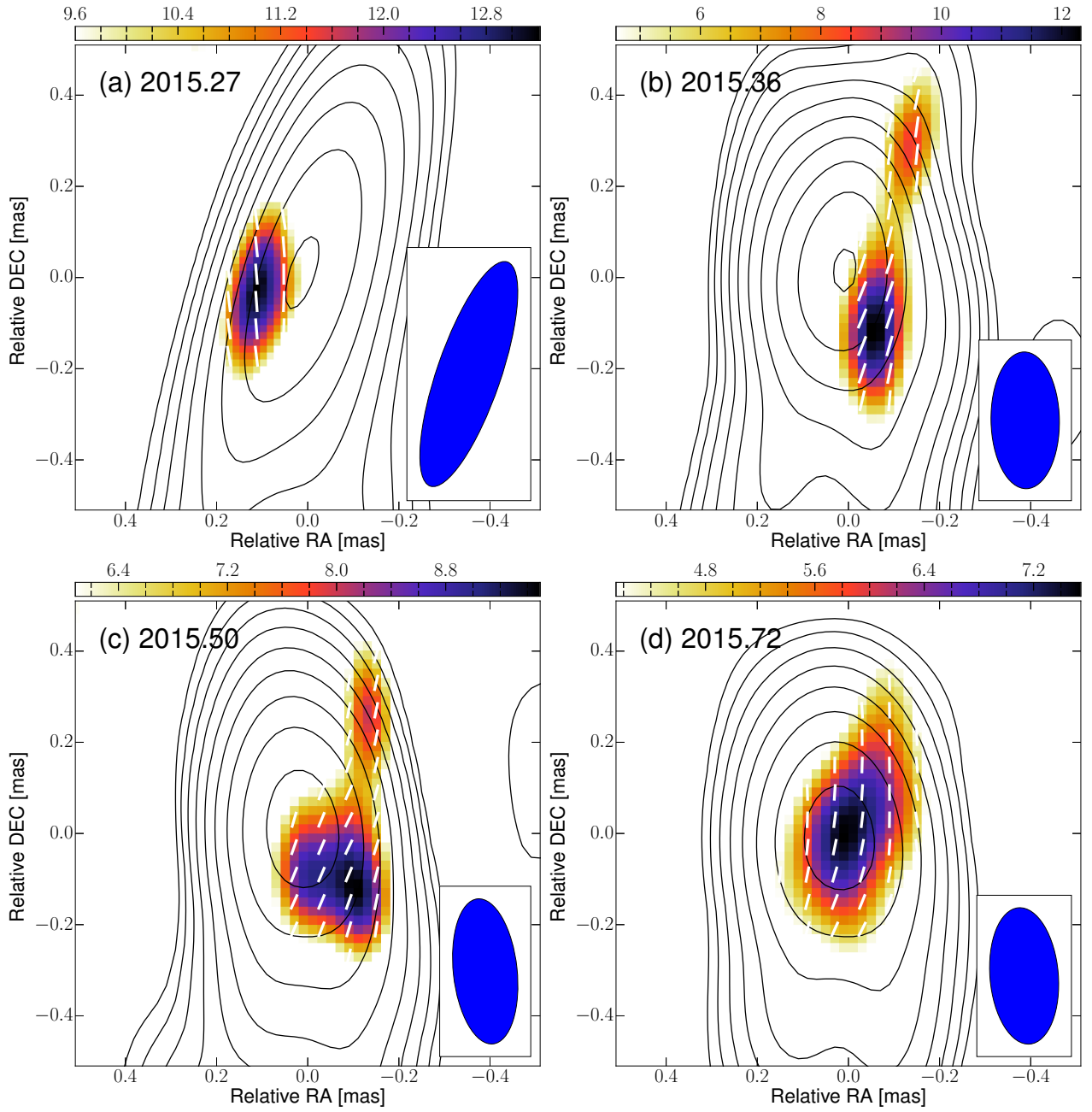


Fig. C.1. VLBA 43 GHz polarization images of 3C 84 zoomed into the core. Labels in the upper left of each panel denotes the observing epoch. The contours show the total intensity and start from 25, 7, 10, and 20 mJy/beam and increase by factor of 2 for the panels (a), (b), (c), and (d), respectively. The colorbar indicates the linear polarization intensity in mJy/beam.